CrossMark

Modeling Nearly Spherical Pure-bulge Galaxies with a Stellar Mass-to-light Ratio Gradient under the ΛCDM and MOND Paradigms. II. The Orbital Anisotropy of Slow Rotators within the Effective Radius

Kyu-Hyun Chae[1] , Mariangela Bernardi[2], and Ravi K. Sheth[2]

[1] Department of Physics and Astronomy, Sejong University, 209 Neungdong-ro Gwangjin-gu, Seoul 05006, Republic of Korea
chae@sejong.ac.kr, kyuhyunchae@gmail.com

[2] Department of Physics and Astronomy, University of Pennsylvania, 209 South 33rd Street, Philadelphia, PA 19104, USA
bernardm@sas.upenn.edu, shethrk@physics.upenn.edu

Abstract

We investigate the anisotropy of the stellar velocity dispersions within the effective radius, R_e, in 24 ATLAS^{3D} pure-bulge galaxies, 16 of which are kinematic slow rotators (SRs). We allow the spherical anisotropy parameter β to be radially varying and allow a radial gradient in the stellar mass-to-light ratio (M_*/L) through the parameter K introduced earlier. The median anisotropy for SRs depends on K as follows: $\langle b_m \rangle = a + bK$ with $a = 0.19 \pm 0.05$, $b = -0.13 \pm 0.07$ (ΛCDM) or $a = 0.21 \pm 0.05$, $b = -0.26 \pm 0.08$ (MOND), where β_m refers to the radially averaged quantity. Under the ΛCDM paradigm, this scaling is tied to a scaling of $\langle f_{DM} \rangle = (0.16 \pm 0.03) + (0.31 \pm 0.06)K$, where f_{DM} refers to the dark matter (DM) fraction within a sphere of $r = R_e$. For $K = 0$ (constant M_*/L), we obtain radially biased results with $\langle b_m \rangle \approx 0.2$, consistent with previous results. However, marginalizing over $0 < K < 1.5$ yields $\langle b_m \rangle = 0.06^{+0.11}_{-0.14}$ with $\langle f_{DM} \rangle = 0.35 \pm 0.08$; isotropy is preferred. This isotropy hides the fact that β_m is correlated with kinematic features such as counterrotating cores (CRCs), kinematically distinct cores (KDCs), and low-level velocities (LVs); SRs with LVs are likely to be radially biased, while SRs with CRCs are likely to be tangentially biased, and SRs with KDCs are intermediate. Existing cosmological simulations allow us to understand these results qualitatively in terms of their dynamical structures and formation histories, although there are quantitative tensions. More realistic cosmological simulations, particularly allowing for M_*/L gradients, may be required to better understand SRs.

Key words: galaxies: elliptical and lenticular, cD – galaxies: evolution – galaxies: formation – galaxies: kinematics and dynamics – galaxies: structure

1. Introduction

Observed galaxies exhibit a great variety in appearances, constituents, and kinematic properties of stars (and gas particles). In galaxies, gravitationally bound stellar orbits can be realized in a number of possible ways, including (rotational) circular orbits, radial orbits, box orbits, tube orbits, irregular/chaotic orbits, etc. (see, e.g., de Zeeuw 1985; Statler 1987; Binney & Tremaine 2008; Röttgers et al. 2014). Based on the overall properties of the orbits, galaxies are broadly referred to as being rotationally supported (or dominated) if circular orbits dominate, as in disk galaxies, or dispersion/pressure-supported (or -dominated) otherwise. Furthermore, a galaxy, whether it is rotation- or dispersion- dominated, can contain several kinematically distinct subsystems, including a rotating disk, a dispersion-supported bulge, and a dispersion-supported dark matter (DM) halo, among others (see, e.g., Binney & Tremaine 2008; Kormendy 2008; Cappellari 2016 and references therein).

The use of integral field spectroscopy (IFS) for kinematic studies of galaxies for the past two decades, led by the SAURON (de Zeeuw et al. 2002) and ATLAS^{3D} (Cappellari et al. 2011) surveys, has revealed crucial aspects and details of the structure and dynamics of early-type (i.e., lenticular and elliptical) galaxies (ETGs; Cappellari et al. 2007, 2013b; Emsellem et al. 2007, 2011; Krajnović et al. 2011). Strikingly, the vast majority of not only lenticular but also elliptical galaxies exhibit varying degrees of rotation (Emsellem et al. 2007, 2011) and also contain disks, as revealed by photometric decomposition (Krajnović et al. 2013). When classified by the angular momentum parameter λ_R introduced by Emsellem et al. (2007), only $14\% \pm 2\%$ of the ATLAS^{3D} sample (36 out of 260) have $l_e < 0.31 \, e_e$ (where ε_e is the ellipticity of the observed light distribution) showing little or no rotation within the effective radius R_e (the half-light radius in the projected light distribution). This minority is referred to collectively as slow rotators (SRs), while the rest are fast rotators (FRs; Emsellem et al. 2011).

The SRs appear nearly round, are relatively more massive, tend to have irregular kinematics (Krajnović et al. 2008, 2011), and do not usually possess detectable disks (Emsellem et al. 2011; Krajnović et al. 2013). The last property means that what appear to be pure bulges on the basis of photometry are likely to be kinematic SRs. In our selection (Chae et al. 2018, hereafter Paper I), two-thirds of the pure bulges (16 out of 24) are SRs. We have carried out spherical Jeans modeling of 24 ATLAS[3D] pure-bulge galaxies to address multiple astrophysical issues, including the radial acceleration relation (RAR) in a supercritical acceleration regime from $\sim 10^{-9.5}$ to $\sim 10^{-8}$ m s^{-2} (Chae et al. 2019), galactic structure, and the distribution of stellar orbits. The last point is the subject of this paper.

All 260 ATLAS[3D] galaxies have been modeled and analyzed through the Jeans anisotropic modeling (JAM) code by the ATLAS[3D] team (Cappellari et al. 2013b). Our modeling (Paper I) is different from the JAM analysis in several ways. First of all, we allow a radial gradient in the stellar mass-to-light ratio ($M_\star/L$); this gradient is confined to the central region ($<0.4~R_e$), with a parameter K representing the strength of a possible gradient. This is motivated by multiple recent reports that the initial mass function (IMF) of stars in the central regions of ETGs is bottom-heavy (e.g., Martín-Navarro et al. 2015; La Barbera et al. 2016; van Dokkum et al. 2017; Sarzi et al. 2018; Sonnenfeld et al. 2018), and this drives a gradient in $M_\star/L$. It should be noted, however, that there are ETGs in which IMF gradients have not been found (e.g., Alton et al. 2017, 2018; Davis & McDermid 2017). Systematic errors in interpreting the relevant spectral features may be responsible for these nonconvergent results, but they may also reflect intrinsic galaxy-to-galaxy variations. Interestingly, Paper I found that posterior inferences of K for the 24 pure bulges exhibit large scatter, with the median strength $\langle K \rangle \sim 0.55$ lying between $K = 1$ and 0, which represent, respectively, the strong gradient reported by van Dokkum et al. (2017) and the case of no gradient at all reported by Alton et al. (2018). It is also interesting to note that the Paper I inference of the gradient for NGC 4486 (M87) agrees well with recent independent studies of the galaxy by Oldham & Auger (2018) and Sarzi et al. (2018).

Second, we allow for radially varying spherical anisotropies β (r) in the stellar velocity dispersions by using a generalized Osipkov–Merritt (gOM; Osipkov 1979; Merritt 1985) model for the region probed by IFS data (typically $r \lesssim R_e$). This was an effort to improve the model fitting of the IFS data but also to investigate possible radial variation that can be compared with theoretical (cosmological hydrodynamic simulation) predictions. Third, in the ΛCDM paradigm (e.g., Mo et al. 2010), the stellar dynamics may be affected by the presence of DM. Whereas the standard lore has been that DM matters little on the small scales currently probed by IFS studies, Bernardi et al. (2018) made the point that if $M_\star/L$ increases toward the center, then this tends to increase the required contribution from DM. Therefore, because we are considering $M_\star/L$ gradients, we allow for different parameterizations of the DM distribution associated with the halo of a galaxy. In what follows, we use DM profiles motivated by Einasto (1965) and Navarro et al. (1997).

Fourth, as there is ongoing discussion (see, e.g., Janz et al. 2016 for a study of some ATLAS[3D] FRs assuming constant $M_\star/L$ and anisotropy) of whether effects attributed to a DM halo can instead be explained by modified Newtonian dynamics (MOND; Milgrom 1983), it is interesting to also consider the MOND paradigm for our study of orbital anisotropies in the presence of M*/L gradients. This is despite the fact that, in these galaxies, the radial acceleration due to baryons ranges from $\sim 10^{-9.5}$ to $\sim 10^{-8}$ m s^{-2} (Chae et al. 2019), which is considerably larger than the critical acceleration, $a_0 \sim 10^{-10}$ m s^{-2}, at which MOND is usually invoked. However, MONDian effects depend on the precise shape of the MOND interpolating function (IF; see Chae et al. 2019), and for some IFs, MONDian effects can be nonnegligible, especially if the $M_\star/L$ gradients in our sample are significant. Hence, we consider two different families of MONDian IFs.

Therefore, here we can constrain the velocity dispersion anisotropies of pure-bulge SRs—which we will refer to as nearly spherical, slowly rotating, pure-bulge galaxies (SSBGs)—in an unprecedented way, taking into account the effects of $M_\star/L$ radial gradients. The velocity dispersion anisotropy is a key parameter characterizing the dynamics of SSBGs and can provide useful constraints on theories of galaxy formation and evolution. As shown in recent state-of-the-art cosmological hydrodynamic simulations (e.g., Naab et al. 2014; Röttgers et al. 2014; Wu et al. 2014; Xu et al. 2017; Li. et al. 2018), as well as galaxy merger simulations (e.g., Balcells & Quinn 1990; Barnes & Hernquist 1996; Jesseit et al. 2005, 2007; Bois et al. 2011; Hilz et al. 2012; Tsatsi et al. 2015) under the ΛCDM paradigm, the assembly history of a galaxy is closely linked with the composition of its stellar orbits, the global angular momentum (i.e., whether it is an FR or SR), and the velocity dispersion anisotropy profile, as well as various morphological and photometric properties. A concise and excellent account of the current state of theoretical ideas and simulations can be found, e.g., in Section 2 of Naab et al. (2014). The SSBGs may look simple, but their present states may be the outcome of complex histories involving in situ star formation, dry (or gasrich) major or minor mergers, and continual accretion and feedback from supernovae and active galactic nuclei (AGNs). Empirically determined velocity dispersion anisotropies may constrain such processes. Simulations (e.g., Röttgers et al. 2014; Wu et al. 2014; Xu et al. 2017) suggest, in particular, that the fraction of in situ stars is well correlated with the anisotropy, in the sense that when the in situ fraction is smaller, the orbital distribution is more dominated by radial orbits (i.e., accreted stars tend to be radially biased).

This paper is structured as follows. In Section 2, we briefly describe the spherical Jeans Monte Carlo (MC) model ingredients that are directly relevant to this work, while referring to Paper I (and also Chae et al. 2019) for details. We present our estimates of the velocity dispersion anisotropies of 16 SSBGs drawn from the ATLAS[3D] sample in Section 3 and show that the $M_\star/L$ radial gradient is a nonnegligible factor in inferring anisotropies from dynamical analyses of SSBGs. In Section 4, we compare our results on the velocity dispersion anisotropy with the predictions by currently available cosmological simulations. We discuss our results and conclude in Section 5.

2. Model Ingredients

In our approach of using the spherical Jeans equation (Binney & Tremaine 2008, Equation (4.215)), we do not construct a library of orbits. Rather, we use the anisotropy parameter

$$\beta = 1 - \frac{\overline{v_q^2} + 2\overline{v_f^2}}{2\overline{v_r^2}} \qquad (1)$$

to gain information about the distribution of orbits at a given point. Here $\overline{v_r^2}$, $\overline{v_q^2}$, and $\overline{v_f^2}$ are the mean squared velocities ("second moments") in the spherical coordinates. These are equivalent to velocity dispersions s_r^2, etc. for nonrotating systems, e.g., the SSBGs considered here. If $\beta > 0$ ($\beta < 0$), the velocity dispersions are radially (tangentially) biased. We allow a radial variation of β even for the relatively small regions ($\lesssim R_e$) probed by the IFS observations in the optical. For this, we use the gOM model (Osipkov 1979; Merritt 1985; see also Binney & Tremaine 2008),

$$\beta_{gOM}(r) = \beta_0 + (\beta_\infty - \beta_0)\frac{(r/r_a)^2}{1 + (r/r_a)^2}, \qquad (2)$$

which varies smoothly from a central value β_0 to β_∞ at large radii. We consider the range [−2, 0.7] for both β_0 and β_∞ so that $1/3 \lesssim s_t^2/s_r^2 \lesssim 3$, where $s_t^2 = (s_q^2 + s_f^2)/2$ is the onedimensional tangential velocity dispersion. For the scale parameter r_a, we consider the range $0 < r_a < R_e$ relevant to the probed region. The model given by Equation (2) is intended to approximate smoothly realistic anisotropy profiles that could be obtained from orbit superposition methods (e.g., Richstone & Tremaine 1988; van der Marel et al. 1998; Gerhard et al. 2001; Gebhardt et al. 2003; Krajnović et al. 2005; Cappellari et al. 2007; Thomas et al. 2007).

The stellar mass distribution in a galaxy is obtained by multiplying the observed light distribution by a stellar mass-tolight ratio $\Upsilon_\star \equiv M_\star/L$. We parameterize this by

$$\frac{\Upsilon_\star(R/R_e)}{\Upsilon_{\star 0}} = \max\{1 + K A[B - R/R(e)], 1\}, \qquad (3)$$

where R is a separation projected along the line of sight onto the plane of the sky, and $(A, B) = (2.33, 6.00)$ is derived by Bernardi et al. (2018) for the recently observed $M_\star/L$ gradient (van Dokkum et al. 2017). Current observational results (e.g., Martín-Navarro et al. 2015; La Barbera et al. 2016; van Dokkum et al. 2017; Alton et al. 2018; Sarzi et al. 2018; Sonnenfeld et al. 2018) correspond to the range $0 \lesssim K \lesssim 1$. In what follows, we consider two separate analyses: one in which there is no gradient (K = 0) and another in which K is allowed to be in the range [0, 1.5].

The JAM modeling results of the ATLAS[3D] ETGs, based on the assumption of constant $M_\star/L$ (K = 0 in our language), show that the inner regions within R_e are dominated by baryons with a median DM fraction of ∼13% within a spherical radius of R_e (Cappellari et al. 2013b). However, as pointed out by Bernardi et al. (2018), if $M_\star/L$ increases toward the center (K > 0 in our language) due to a radial variation in stellar populations or IMF, then one expects larger DM fractions to be required. This is because the change in the baryon distribution (by the radial variation of $M_\star/L$) necessarily requires an adjustment in the DM distribution to obtain the correct total mass distribution for the observed stellar dynamics (velocity dispersions here). That is to say, analyses that assume K = 0 underestimate the importance of a DM halo in the observed stellar dynamics within R_e.

2.1. DM Models

We consider two classes of models that can describe the smooth distribution of DM. These are generalizations of the DM-only simulation prediction (e.g., Navarro et al. 1997; Merritt et al. 2006; Navarro et al. 2010) that would allow for modifications caused by baryonic and feedback physics. One is a generalized Navarro–Frenk–White (gNFW) density profile,

$$\rho_{gNFW}(r) = \frac{\rho_s}{(r/r_s)^\alpha (1 + r/r_s)^{3-\alpha}}, \qquad (4)$$

where −α is the inner density power-law slope (α = 1 being the NFW case) and r_s is the scale radius. We consider the range $0.1 < \alpha < 1.8$. The other is the Einasto profile, $\rho_{Ein}(r) = \rho_{-2} \exp\{(-2/\tilde{\alpha})[(r/r_{-2})^{\tilde{\alpha}} - 1]\}$, (5) where r_{-2} is the radius at which the logarithmic slope of the density is −2 and controls the slope variation with radius along with $\tilde{\alpha}$ as follows: $\gamma_{Ein} \equiv d \ln \rho_{Ein}(r)/d \ln r = -2(r/r_{-2})^{\tilde{\alpha}}$.

Here N-body simulations give $0.15 \lesssim \tilde{\alpha} \lesssim 0.2$ (e.g., Merritt et al. 2006; Navarro et al. 2010). Matching the NFW profile with the Einasto profile with $\tilde{\alpha} = 0.17$, we obtain the radius where the slope is −1 as $r_{-1}/r_{-2} = 0.017$. Now the slope at this fiducial radius $r_{-1} = 0.017 r_{-2}$ is related to $\tilde{\alpha}$ as $\tilde{\alpha} = \ln(-\gamma_{Ein}/2)/\ln 0.017($

). In obtaining an MC set of models, we take a uniform deviate of γ_{Ein} from (0.1, 1.8), which corresponds to a range $0.025 < \tilde{a} < 0.74$, rather than taking $\tilde{a}$ directly from the range, as it will be biased against smaller values of $\tilde{a}$.

2.2. MONDian Models

Models in the MOND paradigm are distinguished by the relation $a/a_B = f(a_B/a_0)$, where a is the actual acceleration, a_B is the acceleration predicted by the distribution of baryons (stars here) based on Newtonian dynamics, and $a_0 \approx 1.2 \times 10^{-10}$ m s^{-2} is the critical acceleration. The function $f(a_B/a_0)$ is known as the IF, and we consider two families of IFs. One is given by

$$ f_n(x) = \frac{1}{2} + \sqrt{\frac{1}{4} + \frac{1}{x^{1/n}}} \Big)^n , \qquad (6) $$

with $0 < \nu \leq 2$, which includes the simple ($\nu = 1$; Famaey & Binney 2005) and standard ($\nu = 2$; Kent 1987) IFs. The other is given by

$$ f(x) = \frac{1}{(1 - e^{-x^{1/2}})^{1/\lambda}} , \qquad (7) $$

with $0.3 < \lambda < 1.7$, which includes McGaugh's IF ($\lambda = 1$; McGaugh 2008).

3. Results

The galaxies selected from the ATLAS^{3D} sample are listed in Table 1. As described in Paper I, photometric decomposition analyses detect no disks in any of these galaxies (Krajnović et al. 2013), so we refer to them as pure bulges. Two-thirds (17/24) have low ellipticities, $\varepsilon_e \leq 0.2$, within R_e (Table 1); the mean ellipticity for all 24 galaxies is $\langle e_e \rangle = 0.184$. In this sense, these galaxies are referred to as nearly round (or spherical). Two-thirds (16/24) are kinematic SRs within R_e, dramatically different from the overall statistics of just 14% (36/260) of SRs from the entire ATLAS^{3D} sample. We analyze these 24 pure bulges using the spherical Jeans equation, paying particular attention to the 16 SRs.

In what follows, we study four different assumptions about the $M_\star/L$ gradient (parameterized by K) and velocity dispersion anisotropy (β):

(a) $K = 0$ (no $M_\star/L$ gradient) and $\beta = $ constant;
(b) $K = 0$ and $\beta = \beta_{gOM}(r)$; (c) $0 < K < 1.5$ and $\beta = $ constant; and (d) $0 < K < 1.5$ and $\beta = \beta_{gOM}(r)$.

Thus, for our most general case (d), a spherical model with a gNFW DM halo (Equation (4)) has six free parameters, i.e., i_0, K, α, β_0, $b_\ast$, and r_a, as well as the following constrained parameters: M_{200} (halo mass), $c = r_{200}/r_s$ (halo concentration), and M_{BH} (black hole mass; see Paper I and Chae et al. 2019 for further details). The number of free parameters is reduced for cases (a) and (b), where we set $K = 0$, and for (a) and (c) when we set $\beta = $ constant.

Table 1
Observed Properties of the ATLAS^{1D} Pure-bulge Galaxies and Quality of Fit to the Spherical Model with the gNFW DM Halo in the ΛCDM Paradigm

Galaxy (a)	ε_e	$\log_{10} s_e$	$\log_{10} s_{e/8}$	$h_{<0.2R_e}$	η_{LW}	Kinematic Feature	n	Case: (b)	(c)	(d)
								χ^2/N_{dof} ("Reduced χ^2")		
	(1)	(2)	(3)	(4)	(5)	(6)	(7)	(8)		
NGC 0661	0.306	2.251	2.279	-0.010 ± 0.032	-0.031	S: NRR/CRC	20	1.2	1.2	1.3	1.4
NGC 1289	0.393	2.095	2.133	$+0.021\pm0.017$	-0.042	S: NRR/CRC	10	1.0	1.3	1.2	1.7
NGC 2695	0.293	2.257	2.342	-0.247 ± 0.023	-0.094	F: RR	23	23.6	2.9	15.2	1.3
NGC 3182	0.166	2.052	2.060	-0.167 ± 0.025	-0.009	F: RR	20	5.2	2.3	4.3	2.5
NGC 3193	0.129	2.252	2.299	-0.083 ± 0.008	-0.052	F: RR	24	2.0	2.1	2.0	2.2
NGC 3607	0.185	2.315	2.360	-0.020 ± 0.004	-0.050	F: RR	34	1.3	0.8	1.7	0.9
NGC 4261	0.222	2.424	2.469	-0.065 ± 0.005	-0.050	S: NRR/NF	32	3.8	1.2	1.4	1.2
NGC 4365	0.254	2.345	2.408	-0.083 ± 0.002	-0.070	S: NRR/KDC	32	10.1	5.5	5.7	4.4
NGC 4374	0.147	2.412	2.460	-0.079 ± 0.002	-0.053	S: NRR/LV	33	2.8	2.6	2.6	2.7
NGC 4406	0.211	2.280	2.336	-0.055 ± 0.001	-0.062	S: NRR/KDC	34	7.2	0.9	1.4	0.9
NGC 4459	0.148	2.199	2.252	-0.105 ± 0.005	-0.059	F: RR	30	7.2	6.3	2.4	2.4
NGC 4472	0.172	2.398	2.460	-0.050 ± 0.001	-0.069	S: NRR/CRC	31	1.7	1.4	1.4	1.5
NGC 4486	0.037	2.422	2.497	-0.138 ± 0.002	-0.083	S: NRR/LV	34	13.9	6.0	2.9	2.6
NGC 4636	0.094	2.259	2.300	-0.023 ± 0.002	-0.045	S: NRR/LV	33	1.7	1.5	1.7	1.5
NGC 4753	0.213	2.241	2.263	-0.023 ± 0.002	-0.045	S: NRR/LV	34	9.7	3.7	9.3	2.7
NGC 5322	0.307	2.351	2.395	$+0.012\pm0.006$	-0.049	S: NRR/CRC	26	1.9	1.2	1.9	1.3
NGC 5481	0.214	2.085	2.174	-0.263 ± 0.032	-0.099	S: NRR/KDC	11	2.7	2.8	1.9	2.6
NGC 5485	0.171	2.223	2.253	-0.091 ± 0.013	-0.033	F: NRR/NF	19	4.6	2.6	3.2	2.5
NGC 5557	0.169	2.306	2.406	-0.185 ± 0.015	-0.111	S: NRR/NF	32	2.7	1.5	1.3	1.4
NGC 5631	0.127	2.176	2.207	-0.097 ± 0.013	-0.034	S: NRR/KDC	24	2.7	1.5	2.2	1.7
NGC 5831	0.136	2.158	2.220	-0.058 ± 0.007	-0.069	S: NRR/KDC	23	2.4	2.1	1.9	2.1
NGC 5846	0.062	2.349	2.365	-0.033 ± 0.003	-0.018	S: NRR/LV	31	2.6	2.6	2.3	2.3
NGC 5869	0.245	2.224	2.260	-0.146 ± 0.011	-0.040	F: RR	19	1.9	2.1	2.0	2.2
NGC 6703	0.019	2.178	2.260	-0.072 ± 0.009	-0.091	S: NRR/LV	30	2.8	1.4	2.4	1.4
							$N_{dof} =$	$n-3$	$n-5$	$n-4$	$n-6$

Note.—Four different assumptions about the $M_\star/L$ gradient (parameterized by K) and velocity dispersion anisotropy (β) are considered: (a) $K=0$ (no $M_\star/L$ gradient) and $\beta=$ constant; (b) $K=0$ and $\beta=\beta_{gOM}(r)$; (c) $0<K<1.5$ and $\beta=$ constant; and (d) $0<K<1.5$ and $\beta=\beta_{gOM}(r)$. (1) Ellipticity of the observed surface brightness distribution within R_e taken from Cappellari et al. (2013b). (2) $\sigma_e=$ the effective velocity dispersion, i.e., the light-weighted $s_{los}(R)$ within R_e, in km s^{-1} taken from Cappellari et al. (2013b). (3) $\sigma_{e/8}=$ the central velocity dispersion, i.e., the light-weighted $s_{los}(R)$ within $R_{e/8}$, in km s^{-1} taken from Cappellari et al. (2013a). (4) $h_{<0.2Re}=$ the logarithmic slope of the $s_{los}(R)$ profile within $R<0.2 R_e$. (5) $\eta_{LW}=$ the logarithmic slope between $R_e/8$ and R_e of the light-weighted (and integrated) values of $s_{los}(R)$ as given in this table. (6) Slow(S)/fast(F) rotator identifications within R_e come from Emsellem et al. (2011). Kinematic features come from Krajnović et al. (2011). The acronyms mean the following (see the text for further details): RR, regular rotator; NRR, nonregular rotator; KDC, kinematically distinct core; CRC, counterrotating core (which is a special case of KDC); LV, low-level (rotation) velocity; NF, no feature. Only one NRR (NGC 5485) is classified as an FR. (7) $n=$ the number of the measured $s_{los}(R)$ values, i.e., the number of the bins in R. (8) Minimum values of the "reduced χ^2," i.e., χ^2 per the number of the degree of freedom (N_{dof}) for the four different cases considered. The N_{dof} for each case is indicated in the last row. A value of $\chi^2/N_{dof}=1$ means that the measured $\sigma_{los}(R)$ values are matched within $\sim1\sigma$, 4 means $\sim2\sigma$, etc. For the most realistic case of (d), all galaxies but NGC 4365 have $\chi^2/N_{dof}\lesssim2.7$, meaning that the measured $\sigma_{los}(R)$ are matched within $\sim1.6\sigma$.

In each case, the model is fitted to the line-of-sight velocity dispersion[3] radial profile, $s_{los}(R)$, constructed from the velocity dispersion map. We do this by minimizing

$$ c^2 = \sum_n \left| \frac{s_{obs} - s_{mod}}{ } \right|_2 $$

$$ \sum_{i=1}^{n} \left[\frac{s_{los}^{obs}(R_i) - s_{los}^{mod}(R_i)}{s_i} \right]^2 , \qquad (8) $$

where $s_{los}^{obs}(R_i)$ and $s_{los}^{mod}(R_i)$ refer to the observed and predicted velocity dispersions at the projected radii R_i, s_i are the observational uncertainties, and n is the number of radial bins as given in Table 1. The number of the degree of freedom (N_{dof}) for each model is then given by $N_{dof}=n-N_{free}$, where N_{free}

---

[1] In Paper I, we referred to this using the acronym "LOSVD" for "line-of-sight velocity dispersion."

is the number of free parameters ranging from 3 to 6. We call $\bar{c}^2 \equiv c^2 N_{\mathrm{dof}}$ the "reduced χ^2."

For each galaxy, we produce a set of 400 MC models for the case of $K = 0$ (constant $M_{\mathring{a}}/L$) and a set of 800 MC models when we allow $0 < K < 1.5$. The MC models for each galaxy are produced iteratively based on Equation (8) from the prior ranges of the model parameters. The details of this procedure can be found in Paper I and Chae et al. (2019). Chae et al. (2019) further described the distribution of $\bar{c}^2$ in the MC set and the fitted $s_{\mathrm{los}}(\ )R$ profiles. Each MC set provides posterior probability density functions (PDFs) of the free parameters. Note that, although we are using the gOM model (Equation (2)) to describe the anisotropy profile, we also produce results for the case of constant anisotropies to quantify the effects of varying anisotropies and provide a direct comparison with relevant previous literature.

3.1. Quality of Fits

Table 1 summarizes the fit qualities of the aforementioned

within $0 < K < 1.5$—the measured line-of-sight velocity dispersions of all 24 galaxies (with the exception of NGC 4365) are matched within $\sim$1.6σ by the best-fitting models. In other words, the reduced χ^2 has minimum values $\bar{c}^2 \Box 2.7$ for the 23 galaxies with an average of $\acute{a}\bar{c}^2\tilde{n} = 1.87$, while NGC 4365 has $\bar{c}^2 = 4.4$ (these values are somewhat different from and meant to replace the values given in Figure 6 of Paper I because we have revised MC samples and corrected N_{dof} here).

However, for the simplest, most restrictive case (a)—spatially constant anisotropy and no $M_{\mathring{a}}/L$ gradient—which has sometimes been adopted in the literature, eight galaxies have unacceptably large $\bar{c}^2 > 4$, and only 15 have $\bar{c}^2 \Box 2.8$. If an $M_{\mathring{a}}/L$ gradient is allowed with $0 < K < 1.5$ for the constant anisotropy model, then four galaxies (NGC 2695, 3182, 4365, and 4753) have $\bar{c}^2 > 4$. If the varied anisotropy model is used with $K = 0$, then three galaxies (NGC 4365, 4459, and 4486) have $\bar{c}^2 > 4$. For these three galaxies, the fit is clearly improved if we allow $K > 0$. Figure 1 illustrates this point for NGC 4486 (M87). This means that, for these galaxies, reasonable gradients
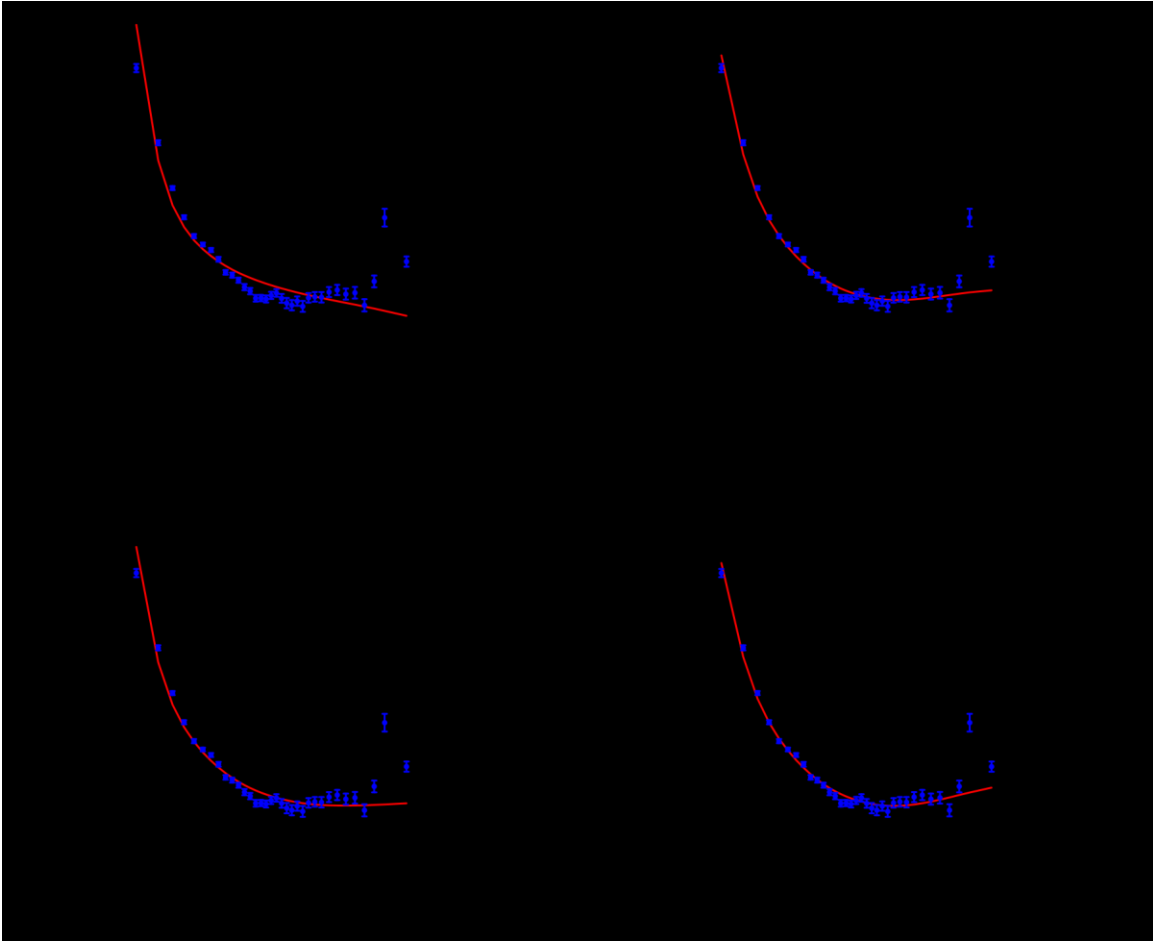

Figure 1. Comparison of the observed $s_{\mathrm{los}}(R)$ profile of NGC 4486 with the best-fit model predictions for the four different cases of Table 1. Note that successful fits can be achieved only for cases (c) and (d), for which an $M_{\mathring{a}}/L$ radial gradient is allowed.

four different cases under the ΛCDM paradigm with the gNFW DM halo model (Equation (4)). For the most general and realistic case (d)—the gOM model with K allowed to vary

in $M_{\mathring{a}}/L$ suffice to explain the current data without invoking drastically varying anisotropies (see, e.g., the classical discussion in Binney & Mamon 1982). In particular, our

conclusion for NGC 4486 agrees with that of Oldham & Auger (2018). For the others, the fit for $0 < K < 1.5$ is as good as or better than that for $K = 0$. What is more significant is that the PDFs of K do not in general prefer $K = 0$, meaning that $K = 0$ should not be presumed unless independent observational constraints require it. Therefore, in inferring the orbital anisotropies, $M_\star/L$ gradients should be allowed.

3.2. Inferred Anisotropy

Figure 2 exhibits the constrained anisotropy values with respect to σ_e, the effective velocity dispersion within R_e from ATLAS[3D] (Cappellari et al. 2013b), and the constrained stellar mass, $M_\star$ (corresponding to the MGE light distribution; see Paper I) for the four different cases of Table 1. Table 2 gives the numerical values of the fitted anisotropies, while Table 3 gives $M_\star/L$ with respect to the SDSS r-band luminosity (Cappellari et al. 2013b). The median value for each case is derived from the composite PDF of the individual PDFs with a uniform weighting. Its statistical uncertainty is estimated from an MC method using the composite PDF. For cases (b) and (d), the composite PDFs are displayed in Figure 3. For these cases with the gOM model, we consider a radially averaged value given by

$$\bar{\beta} \equiv \int_0^{r^{max}} \beta(r)\, dr / r_{max}, \qquad (9)$$
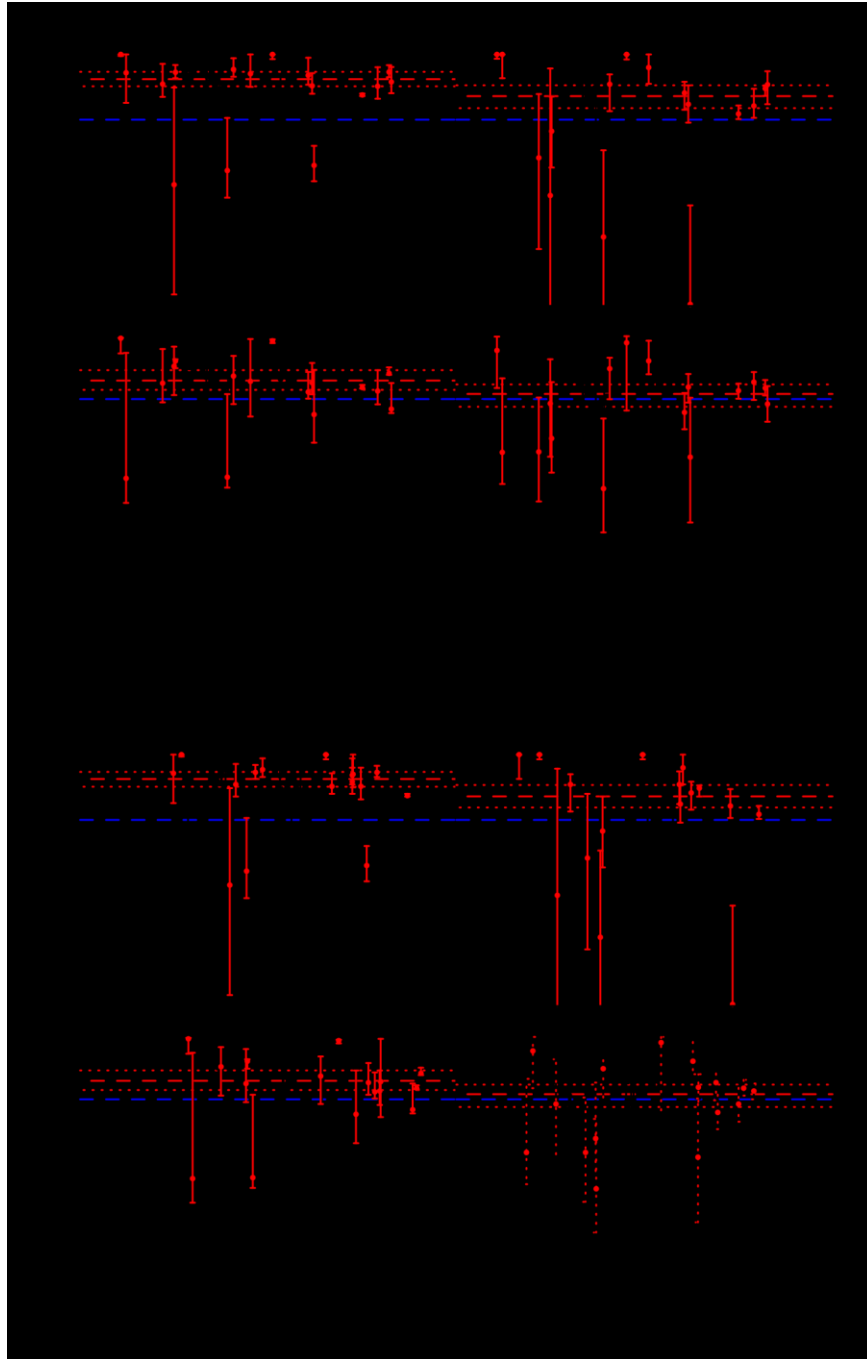
Figure 2. Fitted anisotropies with respect to the effective velocity dispersion σ_e (upper panel) and the fitted stellar mass $M_\ast$ (lower panel) of the 24 ATLAS[3D] pure bulges. The red points represent 16 SSBGs. The red dashed line is the median estimated from the composite PDFs, whose examples are shown in Figure 3. The red dotted lines are the 68% uncertainties of the medians. Four different cases of Table 1 are considered. The numerical values are provided in Tables 2 and 3.

where r_{max} is the maximum radius of the constructed $s_{los}(\ )R$ profile ($\sim R_e$).

We see that the inferred anisotropies depend on the assumption on the anisotropy profile and $M_\ast/L$ gradient. For the cases of constant $M_\ast/L$ ($K=0$), the median anisotropies are radially biased with $\langle b \rangle = 0.43 \pm 0.08$ (for the constant anisotropy; case (a)) or $\langle b_m \rangle = 0.20^{+0.11}_{-0.10}$ (for the gOM anisotropy; case (b)). The former result (case (a)) agrees well with an estimate 0.45 ± 0.25 from the combined analysis of lensing and stellar dynamics by Koopmans et al. (2009) under

the same assumption. The latter result (case (b)) also agrees well with the literature results. Gerhard et al. (2001) obtained a median value of $\beta_m \approx 0.2$ within R_e (their Figure 5) through an orbit superposition modeling of 21 nearly round and slowly rotating galaxies assuming spherical galaxy models. Cappellari et al. (2007) presented various anisotropy parameters based on axisymmetric dynamical modeling of 24 SAURON ETGs. For three SRs in common with our galaxy sample, the spherical anisotropy in Table 2 of Cappellari et al. (2007) is $\beta_m = 0.11$ (NGC 4374), $\beta_m = 0.24$ (NGC 4486), and $\beta_m = 0.17$ (NGC

5846). All are in good agreement with our results for case (b), shown in Table 2.

Figures 2 and 3 indicate that for $0 < K < 1.5$, the anisotropy distribution has a larger spread compared with the case for

Table 2
Fitted Anisotropies of Various Cases with the gNFW DM Model

Galaxy	(a) β	(b) βm	(b) β0	(c) β	(d) βm	(d) β0
NGC 0661	-0.55.+0.290.56	-0.84.+0.110.89	-0.22.+0.200.50 -2.00-+0.002.46	-1.26.+0.70.934	-0.96.+0.470.75 -	-0.15-+1.540.85
NGC 1289	0.50-+0.320.20	-0.85.+0.261.35		0.70-0.250.00	0.57.+0.340.79	
NGC 2695	0.70-+0.000.00	0.20-+0.00.010	-2.00.+0.000.00	0.70-+0.000.00	-0.10.+0.080.15	-2.00-+0.001.73
NGC 3182	-0.96.+0.701.12	-0.17.+0.160.24	0.70-+0.000.00	-2.00.+0.001.76	-0.24.+0.730.22	-2.00-+0.000.33
NGC 3193	0.07-+0.150.22 0.17-+0.240.29	0.25-+0.200.20	0.15-+0.180.18	-1.05.+0.900.92	-0.33.+0.790.45	0.70-+1.900.00
NGC 3607	0.41-+0.120.16	0.21-+0.440.26	0.52-+0.170.18	-0.26.+0.170.33	0.25-+0.140.18	-0.63-+0.860.60
NGC 4261	0.48-+0.100.19	-0.11.+0.040.28	0.34-+0.020.07	0.38-+0.210.14 0.29-+0.180.12	-0.05.+0.190.19	0.19-+0.160.22
NGC 4365	0.36-+0.130.20	0.08-+0.070.22 0.09-+0.140.22	0.26-+0.030.14	0.15-+0.130.18 0.70-+0.050.00	-0.14.+0.180.21	0.26-+0.110.08
NGC 4374	0.49-+0.10.214	0.19-+0.380.45	0.24-+0.040.09	-1.40.+0.470.63	0.18-+0.190.11	0.08-+0.100.12
NGC 4406	0.39-+0.10.130	0.45-+0.130.10	0.38-+0.170.32	0.06-0.060.09	0.61-+0.730.07	0.17-+0.160.09
NGC 4459	0.26-+0.010.02	0.12-+0.010.03	0.41-+0.130.10	0.34-+0.080.03	-1.42.+0.360.58	0.64-+0.410.06
NGC 4472	0.51-+0.060.07	0.28-+0.020.06	0.15-+0.010.02	0.38-+0.290.11	0.09-+0.090.08	-1.38-+0.620.51
NGC 4486	0.54-+0.080.12 0.47-+0.120.22	0.25-+0.300.22	0.45-+0.000.01	-0.25.+0.630.61	0.12-+0.080.09	0.09-0.080.05
NGC 4636	-0.49.+0.170.21	0.44-+0.060.07	0.43-+0.040.08	-1.98.+0.021.06	0.33-+0.330.12	0.33-+0.080.04
NGC 4753	0.70-+0.020.00 0.47-+0.100.12	-0.16.+0.300.48	0.32-+0.060.08	0.70-+0.050.00	-0.07.+0.280.29	0.40-+0.110.06
NGC 5322	0.70-+0.050.00	0.65-+0.160.00	-0.38.+0.270.49	0.33-+0.360.26	-0.62.+0.700.64	-0.49-+0.360.48
NGC 5481	-0.70.+1.181.04	0.13-+0.030.12	0.70-+0.810.00	0.56-+0.180.14	0.52-+0.40.150	-1.10-+0.900.76
NGC 5485	0.38-+0.140.22	0.63-+0.030.01	0.46-+0.010.02	-0.81.+1.191.36	-0.03.+0.210.19	0.41-+0.600.29
NGC 5557	0.36-+0.090.14	0.35-+0.310.21	0.70-+0.000.00	-0.41.+0.980.69	0.41-+0.140.22	0.33-+0.170.10
NGC 5631	0.48-+0.110.22	0.17-+0.210.37 0.18-+0.120.21	0.70-+0.000.00	0.17-+0.200.20	-0.05.+0.570.48	0.65-+0.060.05
NGC 5831	0.51-+0.060.08	0.36-+0.150.29	0.26-+0.130.30	-0.18.+0.540.49	-0.57.+0.530.58	-0.12.+0.810.74
NGC 5846		0.41-+0.080.02	0.28-+0.060.14	-0.12.+0.390.37	0.13-+0.170.14	-0.61-0.400.66
NGC 5869			0.43-+0.070.24		-0.06.+0.420.36	0.18-+0.130.11
NGC 6703			0.08-+0.350.12		-0.42.+0.370.60	0.04-+0.410.30
						-1.80-+0.201.38

Note．Fitted anisotropy values for the four different cases of Table 1. For cases (b) and (d), the parameters βm and β0, respectively, refer to the radially averaged value

and the central value of the fitted gOM model (Equation (2)).

$K = 0$. This appears to be a consequence of the shift of the anisotropy values for selective galaxies to lower values for $0 < K < 1.5$ from the case for $K = 0$. The second panels from the top in Figure 3 show that the PDF for the lower-σ_e galaxies for $0 < K < 1.5$ has a larger spread than that for $K = 0$. On the other hand, the PDF for higher-σ_e galaxies does not show a significant shift between the two cases.

Comparison of case (b) with case (a) shows that for many galaxies with unacceptable fits when the anisotropy is assumed constant (see Table 1), the introduction of radially varying anisotropies can improve the fit dramatically, qualitatively consistent with dynamical modeling results (e.g., Gerhard et al. 2001; Gebhardt et al. 2003; Thomas et al. 2007). The anisotropy profile $\beta(r)$ inferred for $K = 0$ is shown in Figure 4. While our smooth model may not capture fine details that might be recovered from orbit superposition modeling (e.g., Gerhard et al. 2001; Gebhardt et al. 2003; Thomas et al. 2007), it appears to capture overall radial trends within the relatively central optical regions. We find both radially increasing and declining $\beta(r)$. Note, however, for several galaxies (NGC 4365, 4459, 4486, and 4753), if we fix $K = 0$, then the fit quality is still not good, even with the radially varying anisotropy model of $\beta_{gOM}(r)$.

When an $M_\ast/L$ gradient is allowed, the fits are improved, sometimes dramatically. Interestingly, even for the constant anisotropy model, the improvement is dramatic, except for four galaxies (NGC 2695, 3182, 4365, and 4753). This implies significant degeneracies between K and anisotropy shape. Nevertheless, to obtain successful fits for all galaxies, we require both $M_\ast/L$ radial gradient and radial variations in β. With the constraint $0 < K < 1.5$, we have $\langle b_m \rangle = 0.25_{-0.13}^{+0.12}$ (for the constant anisotropy; case (c)) or $\langle b_m \rangle = 0.06_{-0.12}^{+0.10}$ (for the gOM anisotropy; case (d)). Compared with the corresponding cases with $K = 0$, the median anisotropies are reduced by $\Delta \langle b_m \rangle \approx -0.2$. Figure 5 shows the anisotropy profiles $\beta(r)$ for $0 < K < 1.5$.

Replacing the gNFW profile with the Einasto form (Equation (5)) yields similarly good fits (i.e., χ^2 values) and anisotropy profiles, so we do not exhibit them. When the MOND models (Equations (6) and (7)) are used, we also obtain similar χ^2 and β. This means that our results are robust with respect to model choices in both the ΛCDM and MOND paradigms.

3.3. Anticorrelation between b and $M_\ast/L$ Gradient

Strikingly, for the most general case (d), isotropic velocity dispersions ($\beta_m = 0$) are preferred. To understand why, we split the MC models for the case of radially varying anisotropy into four bins in K, including the special case of $K = 0$. We then analyze the MC models in each bin and obtain the anisotropies.

The results are displayed in Figure 6, which shows a clear trend for $\langle b_m \rangle$ to decrease as K increases. Combining the two ΛCDM results, i.e., for the gNFW and Einasto profiles, we find

$$\langle b_m \rangle = +a - bK, \tag{10}$$

Table 3
Fitted M$_*$/L and f$_{DM}$(r=R$_e$) of Various Cases with the gNFW DM Model

Galaxy	(a)		(b)		(c)			(d)		
	f_{DM}	$\log_{10} i_{*0}$	f_{DM}	$\log_{10} i_{*0}$	f_{DM}	$\log_{10} i_{*0}$	$\log_{10} i_{*e}$	f_{DM}	$\log_{10} i_{*0}$	$\log_{10} i_{*e}$
NGC 0661	$0.103_{-0.063}^{+0.205}$	$0.911_{-0.111}^{+0.024}$	$0.066_{-0.050}^{+0.205}$	$0.944_{-0.118}^{+0.018}$	$0.237_{-0.129}^{+0.146}$	$0.792_{-0.120}^{+0.074}$	$0.821_{-0.083}^{+0.058}$	$0.211_{-0.154}^{+0.177}$	$0.770_{-0.126}^{+0.132}$	$0.818_{-0.103}^{+0.101}$
NGC 1289	$0.407_{-0.07}^{+0.1514}$	$0.413_{-0.126}^{+0.056}$	$0.208_{-0.103}^{+0.229}$	$0.515_{-0.118}^{+0.019}$	$0.551_{-0.23}^{+0.155}$	$0.251_{-0.31}^{+0.156}$				
NGC 2695						$0.530_{-0.019}^{+0.042}$	$0.274_{-0.262}^{+0.13}$	$0.431_{-0.18}^{+0.196}$	$0.290_{-0.17}^{+0.138}$	$0.331_{-0.13}^{+0.1136}$
NGC 3182	$0.035_{-0.021}^{+0.028}$	$0.592_{-0.014}^{+0.012}$	$0.016_{-0.008}^{+0.009}$		$0.025_{-0.015}^{+0.017}$	$0.252_{-0.29}^{+0.1614}$	$0.599_{-0.01}^{+0.007}$	$0.020_{-0.012}^{+0.013}$	$0.400_{-0.03}^{+0.053}$	$0.474_{-0.01}^{+0.029}$
NGC 3193			$0.284_{-0.189}^{+0.287}$	$0.537_{-0.005}^{+0.006}$		$0.456_{-0.059}^{+0.039}$				
NGC 3607	$0.215_{-0.142}^{+0.445}$	$0.474_{-0.411}^{+0.063}$	$0.131_{-0.086}^{+0.229}$	$0.502_{-0.227}^{+0.311}$	$0.412_{-0.19}^{+0.054}$	$0.491_{-0.13}^{+0.0712}$	$0.336_{-0.292}^{+0.116}$	$0.510_{-0.174}^{+0.214}$	$0.220_{-0.192}^{+0.159}$	$0.295_{-0.189}^{+0.126}$
NGC 4261	$0.091_{-0.05}^{+0.12}$	$0.529_{-0.046}^{+0.018}$	$0.192_{-0.142}^{+0.321}$	$0.482_{-0.126}^{+0.044}$	$0.099_{-0.058}^{+0.095}$	$0.393_{-0.235}^{+0.055}$	$0.489_{-0.04}^{+0.024}$	$0.158_{-0.1}^{+0.212}$	$0.335_{-0.083}^{+0.061}$	$0.395_{-0.128}^{+0.076}$
NGC 4365			$0.111_{-0.075}^{+0.274}$	$0.346_{-0.095}^{+0.168}$		$0.465_{-0.113}^{+0.074}$		$0.431_{-0.125}^{+0.16}$	$0.395_{-0.147}^{+0.077}$	$0.414_{-0.128}^{+0.076}$
NGC 4374	$0.377_{-0.158}^{+0.275}$	$0.511_{-0.257}^{+0.09}$	$0.140_{-0.085}^{+0.198}$	$0.625_{-0.258}^{+0.057}$		$0.688_{-0.097}^{+0.041}$	$0.519_{-0.122}^{+0.048}$	$0.506_{-0.28}^{+0.201}$		$0.741_{-0.233}^{+0.171}$
NGC 4406	$0.530_{-0.153}^{+0.187}$	$0.654_{-0.245}^{+0.121}$	$0.099_{-0.069}^{+0.17}$	$0.700_{-0.04}^{+0.0834}$	$0.346_{-0.095}^{+0.168}$	$0.145_{-0.191}^{+0.062}$	$0.470_{-0.23}^{+0.039}$	$0.341_{-0.254}^{+0.178}$	$0.708_{-0.269}^{+0.197}$	$0.650_{-0.145}^{+0.104}$
NGC 4459	$0.167_{-0.1}^{+0.238}$	$0.663_{-0.133}^{+0.037}$	$0.281_{-0.155}^{+0.419}$	$0.975_{-0.133}^{+0.015}$	$0.744_{-0.164}^{+0.069}$	$0.328_{-0.029}^{+0.075}$	$0.519_{-0.075}^{+0.064}$	$0.337_{-0.195}^{+0.19}$	$0.606_{-0.187}^{+0.123}$	$0.651_{-0.144}^{+0.142}$
NGC 4472	$0.270_{-0.097}^{+0.189}$	$0.724_{-0.13}^{+0.047}$	$0.107_{-0.074}^{+0.154}$	$0.783_{-0.087}^{+0.018}$	$0.449_{-0.132}^{+0.11}$	$0.580_{-0.202}^{+0.088}$	$0.697_{-0.072}^{+0.045}$	$0.761_{-0.371}^{+0.186}$	$0.612_{-0.184}^{+0.166}$	$0.299_{-0.617}^{+0.381}$
NGC 4486	$0.287_{-0.108}^{+0.162}$	$0.605_{-0.116}^{+0.056}$	$0.087_{-0.037}^{+0.058}$	$0.824_{-0.085}^{+0.031}$	$0.290_{-0.06}^{+0.139}$	$0.423_{-0.135}^{+0.058}$	$0.213_{-0.15}^{+0.0634}$	$0.074_{-0.046}^{+0.077}$	$0.243_{-0.622}^{+0.405}$	$0.417_{-0.021}^{+0.039}$
NGC 4636	$0.097_{-0.068}^{+0.123}$	$0.500_{-0.059}^{+0.023}$	$0.087_{-0.06}^{+0.249}$	$0.752_{-0.341}^{+0.082}$	$0.744_{-0.164}^{+0.069}$	$0.116_{-0.499}^{+0.323}$	$0.414_{-0.016}^{+0.042}$	$0.276_{-0.18}^{+0.264}$	$0.330_{-0.031}^{+0.07}$	$0.604_{-0.134}^{+0.088}$
NGC 4753	$0.063_{-0.017}^{+0.025}$	$0.711_{-0.006}^{+0.004}$	$0.105_{-0.07}^{+0.24}$	$0.466_{-0.061}^{+0.043}$	$0.068_{-0.042}^{+0.069}$	$0.233_{-0.104}^{+0.069}$	$0.623_{-0.146}^{+0.069}$	$0.439_{-0.17}^{+0.1114}$	$0.553_{-0.204}^{+0.107}$	$0.728_{-0.186}^{+0.083}$
NGC 5322	$0.306_{-0.149}^{+0.415}$	$0.709_{-0.399}^{+0.075}$	$0.083_{-0.048}^{+0.07}$	$0.760_{-0.01}^{+0.004}$	$0.270_{-0.196}^{+0.279}$	$0.625_{-0.086}^{+0.031}$	$0.491_{-0.13}^{+0.189}$	$0.755_{-0.322}^{+0.18}$	$0.659_{-0.045}^{+0.107}$	$0.362_{-0.543}^{+0.43}$
NGC 5481		$0.479_{-0.295}^{+0.14}$	$0.353_{-0.119}^{+0.229}$	$0.943_{-0.118}^{+0.014}$	$0.626_{-0.074}^{+0.067}$	$0.605_{-0.059}^{+0.067}$	$0.135_{-0.461}^{+0.353}$	$0.290_{-0.545}^{+0.473}$		$0.242_{-0.035}^{+0.026}$
NGC 5485	$0.654_{-0.142}^{+0.15}$ 0.246	$0.279_{-0.307}^{+0.07}$	$0.123_{-0.082}^{+0.225}$	$0.788_{-0.297}^{+0.152}$	$0.852_{-0.303}^{+0.098}$	$0.478_{-0.321}^{+0.093}$	$0.312_{-0.108}^{+0.038}$	$0.171_{-0.069}^{+0.088}$	$0.159_{-0.045}^{+0.065}$	$0.494_{-0.137}^{+0.101}$
NGC 5557	$0.096_{-0.049}^{+0.062}$	$0.680_{-0.022}^{+0.013}$	$0.185_{-0.124}^{+0.437}$	$0.256_{-0.062}^{+0.038}$	$0.205_{-0.109}^{+0.227}$	$0.534_{-0.079}^{+0.055}$	$0.283_{-0.184}^{+0.226}$		$0.441_{-0.14}^{+0.134}$	
NGC 5631	$0.088_{-0.059}^{+0.089}$	$0.702_{-0.033}^{+0.021}$	$0.094_{-0.068}^{+0.206}$ $0.101_{-0.066}^{+0.097}$	$0.623_{-0.146}^{+0.042}$	$0.115_{-0.06}^{+0.113}$	$0.276_{-0.193}^{+0.209}$	$0.646_{-0.059}^{+0.019}$	$0.144_{-0.101}^{+0.138}$	$0.570_{-0.09}^{+0.082}$	$0.639_{-0.064}^{+0.057}$
NGC 5831	$0.500_{-0.155}^{+0.254}$	$0.542_{-0.331}^{+0.121}$		$0.739_{-0.045}^{+0.019}$	$0.142_{-0.098}^{+0.104}$	$0.494_{-0.106}^{+0.083}$	$0.675_{-0.038}^{+0.031}$	$0.284_{-0.193}^{+0.213}$	$0.695_{-0.149}^{+0.132}$	$0.749_{-0.137}^{+0.1}$
NGC 5846	$0.102_{-0.061}^{+0.124}$	$0.636_{-0.052}^{+0.024}$		$0.874_{-0.095}^{+0.021}$	$0.516_{-0.156}^{+0.205}$	$0.526_{-0.216}^{+0.156}$ $0.583_{-0.068}^{+0.084}$	$0.527_{-0.345}^{+0.108}$	$0.104_{-0.066}^{+0.166}$	$0.587_{-0.08}^{+0.067}$	$0.671_{-0.079}^{+0.033}$
NGC 5869	$0.272_{-0.128}^{+0.28}$	$0.535_{-0.213}^{+0.063}$		$0.704_{-0.038}^{+0.028}$	$0.178_{-0.089}^{+0.141}$	$0.578_{-0.057}^{+0.087}$	$0.601_{-0.053}^{+0.035}$	$0.471_{-0.186}^{+0.174}$	$0.269_{-0.153}^{+0.147}$	$0.325_{-0.136}^{+0.12}$
NGC 6703	$0.129_{-0.084}^{+0.208}$	$0.625_{-0.111}^{+0.033}$		$0.516_{-0.183}^{+0.099}$	$0.523_{-0.219}^{+0.187}$		$0.341_{-0.2}^{+0.162}$	$0.172_{-0.109}^{+0.222}$	$0.484_{-0.087}^{+0.128}$	$0.550_{-0.067}^{+0.097}$
	$0.444_{-0.164}^{+0.322}$	$0.674_{-0.518}^{+0.115}$		$0.679_{-0.142}^{+0.036}$	$0.200_{-0.146}^{+0.203}$		$0.563_{-0.089}^{+0.055}$	$0.438_{-0.271}^{+0.217}$	$0.622_{-0.186}^{+0.213}$	$0.672_{-0.178}^{+0.191}$
	$0.100_{-0.072}^{+0.188}$	$0.720_{-0.087}^{+0.023}$		$0.868_{-0.327}^{+0.054}$	$0.587_{-0.179}^{+0.138}$		$0.586_{-0.175}^{+0.134}$	$0.114_{-0.077}^{+0.204}$	$0.575_{-0.079}^{+0.114}$	$0.638_{-0.059}^{+0.079}$
	$0.090_{-0.057}^{+0.084}$	$0.732_{-0.031}^{+0.018}$		$0.756_{-0.109}^{+0.032}$	$0.134_{-0.092}^{+0.166}$		$0.644_{-0.048}^{+0.048}$	$0.128_{-0.078}^{+0.171}$	$0.541_{-0.05}^{+0.088}$	$0.619_{-0.053}^{+0.04}$
				$0.689_{-0.036}^{+0.028}$	$0.115_{-0.077}^{+0.136}$		$0.650_{-0.031}^{+0.044}$			

Note. Fitted values for the four different cases of Table 1. The parameter i_{*0} (Equation (3)) refers to the value of M$_*$/L for the region where M$_*$/L is constant, while i_{*e} is the average M$_*$/L for the projected region within R$_e$, which is, of course, the same as i_{*0} for cases (a) and (b). The parameter f$_{DM}$ refers to the fraction of DM

within the spherical volume of radius $r = R_e$.

with $a = 0.19 \pm 0.05$ and $b = -0.13 \pm 0.07$. We obtain similar coefficients, $a = 0.21 \pm 0.05$ and $b = -0.26 \pm 0.08$, from the MOND results. Clearly, $\beta > 0$ is obtained only if $K \approx 0$, although the bias toward more radial orbits may not be large. As K gets larger than ~0.5, $\beta = 0$ starts to be preferred, while at large $K \gg 1$, a tangential bias ($\beta < 0$) is preferred. As shown in Paper I, our posterior distributions of K give $\langle K \rangle \sim 0.55$ (and hence $\beta \approx 0$). Figure 6 highlights the importance of K in modeling elliptical galaxies.

Therefore, if we accept the existence of M_*/L gradients (see references in the Introduction), then we must conclude that previous spherical Jeans dynamical modeling that ignored gradients is likely to be biased toward larger β, i.e., toward finding more radial anisotropy.

Figure 2 of Bernardi et al. (2018) shows why β and K are expected to be anticorrelated. For the observed $s_{los}( )R$ profile and light distribution, the $s_{los}( )R$ profile cannot generally be fitted by an isotropic velocity dispersion and a constant M_*/L. The observed $s_{los}( )R$ profile can then try to be fitted by a radially varying β or a nonzero K. For example, a $s_{los}( )R$ profile that is rising toward the center can be realized by either a relatively higher β along with a relatively less steep mass profile or a relatively lower β along with a relatively steeper mass profile. As a result, there is a degeneracy between β and K that controls the steepness of the mass profile for the given light profile. Comparison of cases (b) and (c) shows that this degeneracy is in part broken by the observed $s_{los}( )R$ profile in some cases, such as NGC 4486 (Figure 1). Only a $K > 0$ can have the required strong effect in the central region to fit the rising $s_{los}( )R$ profile well. On the other hand, for a case like NGC 4753, whose $s_{los}( )R$ profile is not rising toward the center, a $K > 0$ does not improve the fit, but a radially varying β is required (see Table 1).

This K–β degeneracy is a modern version of the classical mass–anisotropy degeneracy first discussed in Binney & Mamon (1982). The increased precision and spatial resolution that are now available let us study the interplay between the profiles of β, M_*/L, and DM.

3.4. Degeneracy between f_{DM} and M_*/L Gradient

Our analysis has shown that the K–β degeneracy persists even when DM is included. Therefore, we now show what our results imply for the DM distribution.

As Figure 1 of Bernardi et al. (2018) shows, when K is increased (i.e., the M_*/L gradient is stronger), the stellar mass distribution becomes more centrally concentrated, so the DM mass within R_e must increase to fit the observed line-of-sight velocity dispersions outside the central region. In addition, Figures 17 and 18 of Paper I show that the average M_*/L within R_e decreases.

Figure 7 exhibits this expected scaling of the DM fraction f_{DM} (within a sphere of $r = R_e$) with K. Together, the gNFW and Einasto results imply

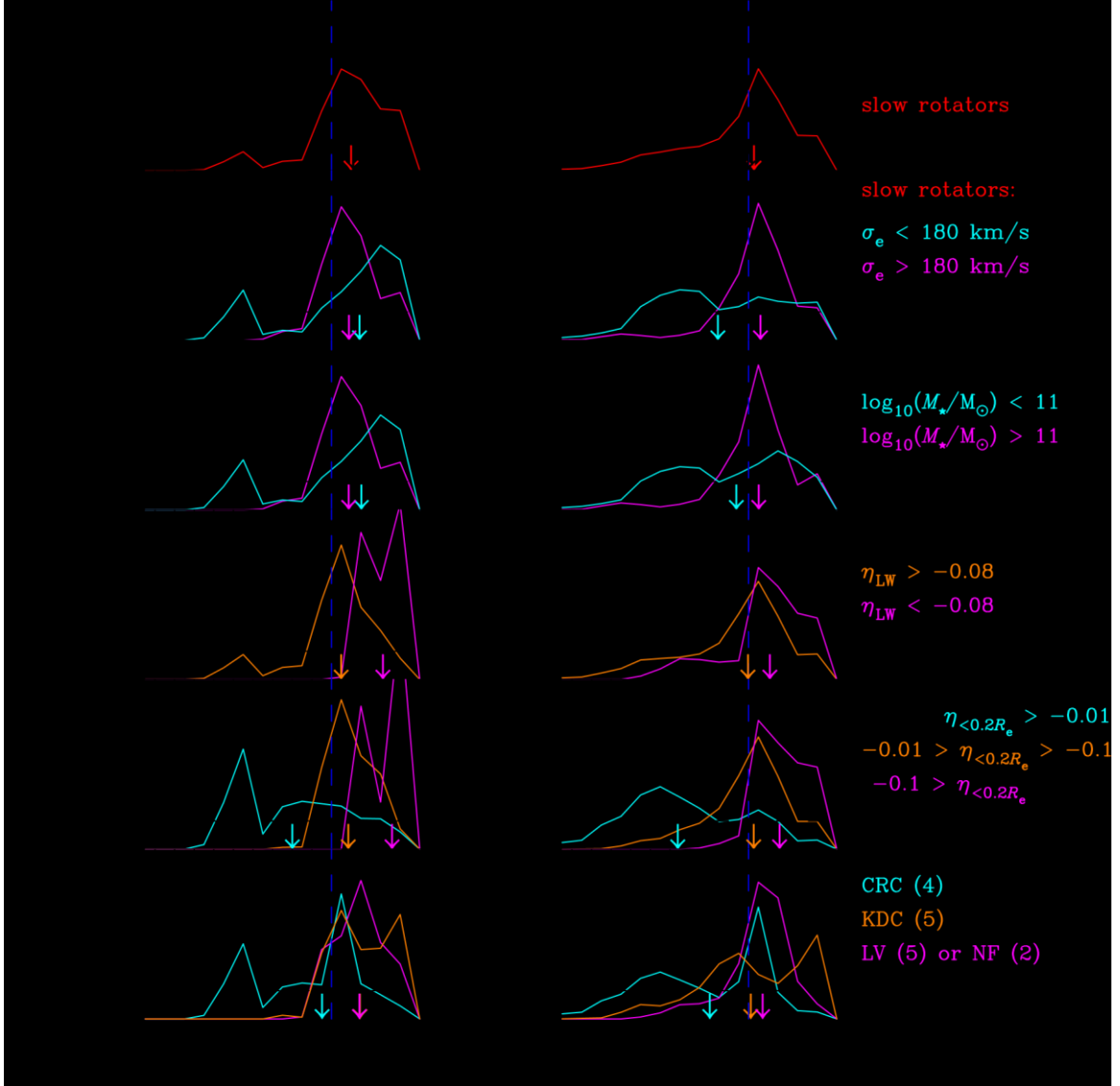$$\langle f_{DM} \rangle = a_f + b\, K_f \; , \qquad (11)$$

with

Figure 3. The PDFs of β_m for the cases of $K=0$ and $0 < K < 1.5$ with the gOM anisotropy model: cases (b) and (d) of Table 1. The top panels show the PDFs for all 24 pure-bulge galaxies (black) and 16 SRs (red). The other panels show the PDFs for subsamples of SRs split, respectively, by σ_e (effective velocity dispersion), $M_\star$ (fitted stellar mass), η_{LW} (logarithmic slope of the light-weighted line-of-sight velocity dispersion $\acute{s}_{los}\tilde{n}(R)$ between $R_e/8$ and R_e), $h_{<0.2R_e}$ (logarithmic slope of the $s_{los}(R)$ profile for $R < 0.2\ R_e$), and kinematic features (see Table 1). The downward-pointing arrows indicate the medians in the PDFs.

$a_f = 0.20 \pm 0.05,\qquad b_f = 0.22 \pm 0.07$ (all)   and
$a_f = 0.25 \pm 0.05,\ b_f = 0.26 \pm 0.07$ (SRs)

when $\beta = $ constant and

$a_f = 0.14 \pm 0.03,\qquad b_f = 0.26 \pm 0.07$ (all)   and
$a_f = 0.16 \pm 0.03,\ b_f = 0.31 \pm 0.06$ (SRs)

when $\beta = \beta_{gOM}(r)$. Marginalizing over K yields
$\acute{a}f_{DM}\tilde{n} = 0.32 \pm 0.09$ (all) and 0.40 ± 0.09 (SRs)

when $\beta = $ constant and

$\acute{a}f_{DM}\tilde{n} = 0.30 \pm 0.08$ (all) and 0.35 ± 0.08 (SRs)

when $\beta = \beta_{gOM}(r)$. These DM fractions are larger than the value $f_{DM} \sim 0.13$ returned by JAM modeling of these galaxies (Cappellari et al. 2013b). However, if we, like they, set $K = 0$, then our analysis also returns $f_{DM} \sim 0.13$ for all pure bulges. Table 3 gives the values of f_{DM}, i_{e} (the average value of $M_{\ast}/L$ within the projected R_e), and i_0 (the constant value at $R > 0.4\ R_e$) for cases (a)–(d) with the gNFW DM model specified in Table 1.

3.5. Implication for MOND

The increased DM fraction in the optical regions when $K \neq 0$ under the ΛCDM paradigm must imply an important modification to the MOND IF compared with the case for $K = 0$. This means that the $M_{\ast}/L$ gradient is a crucial factor in studying the RAR using elliptical galaxies. The reader is referred to Chae et al. (2019) for a detailed discussion of the RAR based on extensive modeling results, including those considered here.

3.6. Correlation of b with Velocity Dispersions

For the most general case, (d), Figures 2 and 3 hint that higher-σ_e ($\sigma_e > 180$ km s^{-1}) and lower-σ_e ($\sigma_e < 180$ km s^{-1}) galaxies may have different anisotropies, as would be expected if their formation histories are different (Xu et al. 2017;
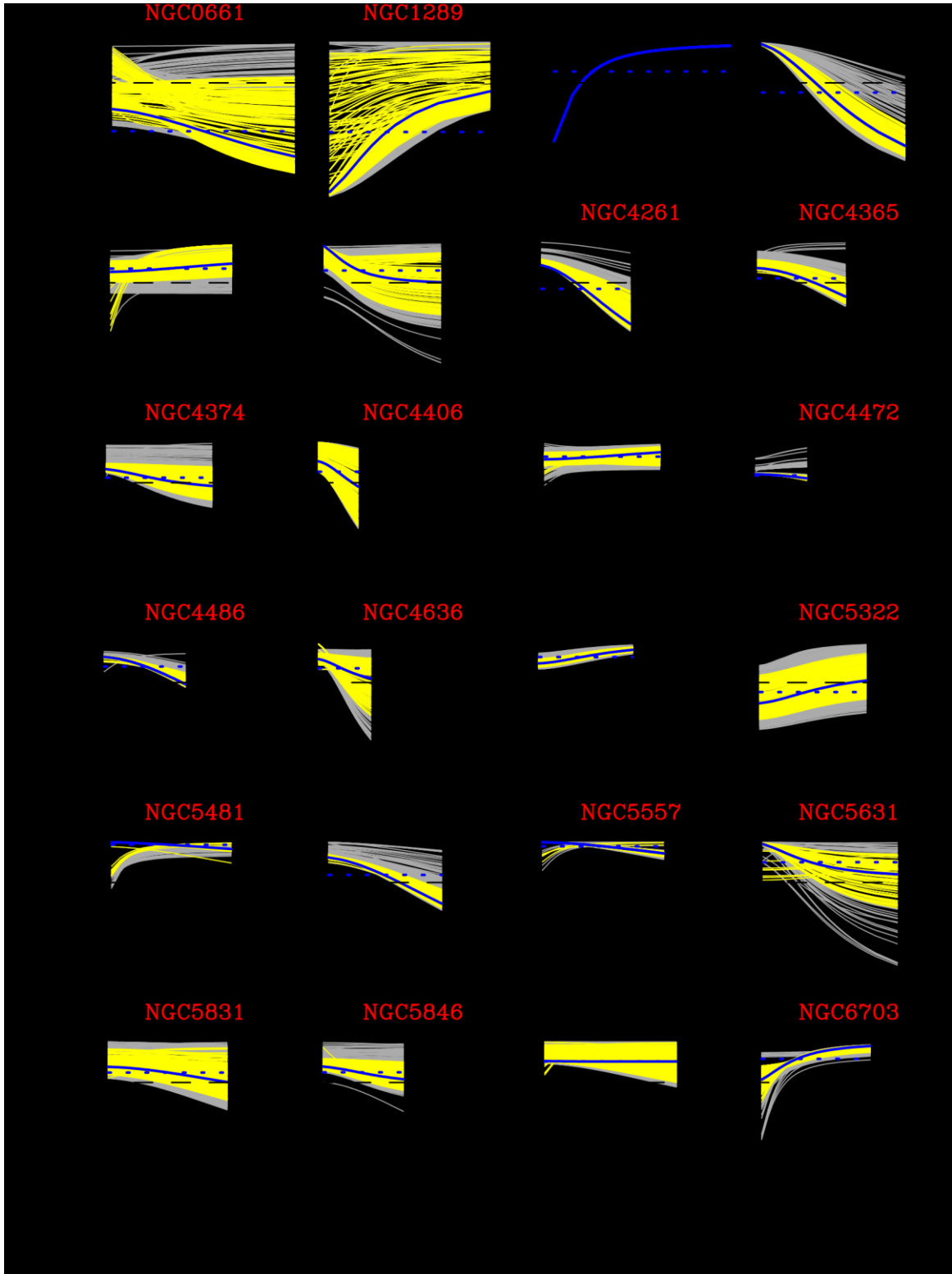
Figure 4. Constrained anisotropy profiles for case (b) of Table 1 (i.e., for K⊡=⊡0). All MC models satisfying $\bar{c}^2 < 2\bar{c}^2_{min}$ are shown (see Paper I). Yellow curves represent only 68% of the models from the median denoted by the blue curve. The blue dotted line shows β_m obtained from this blue curve from Equation (9). For SRs, the galaxy ID is shown in red.

Li et al. 2018). If we consider the central anisotropy parameter β_0, then the dichotomy appears clearer, as shown in Figures 8 and 9. There appears to be a similar dichotomy between the higher stellar mass ($M_a⊡>⊡10^{11} M_e$) subsample and the lower stellar mass ($M_a⊡<⊡10^{11} M_e$) subsample. The higher-σ_e (or M_a) galaxies are likely to be radially biased, while the lower-σ_e (or

Mₐ) galaxies have a significant   3.7.   Correlation of b with the Slope of $s_{los}(R)$
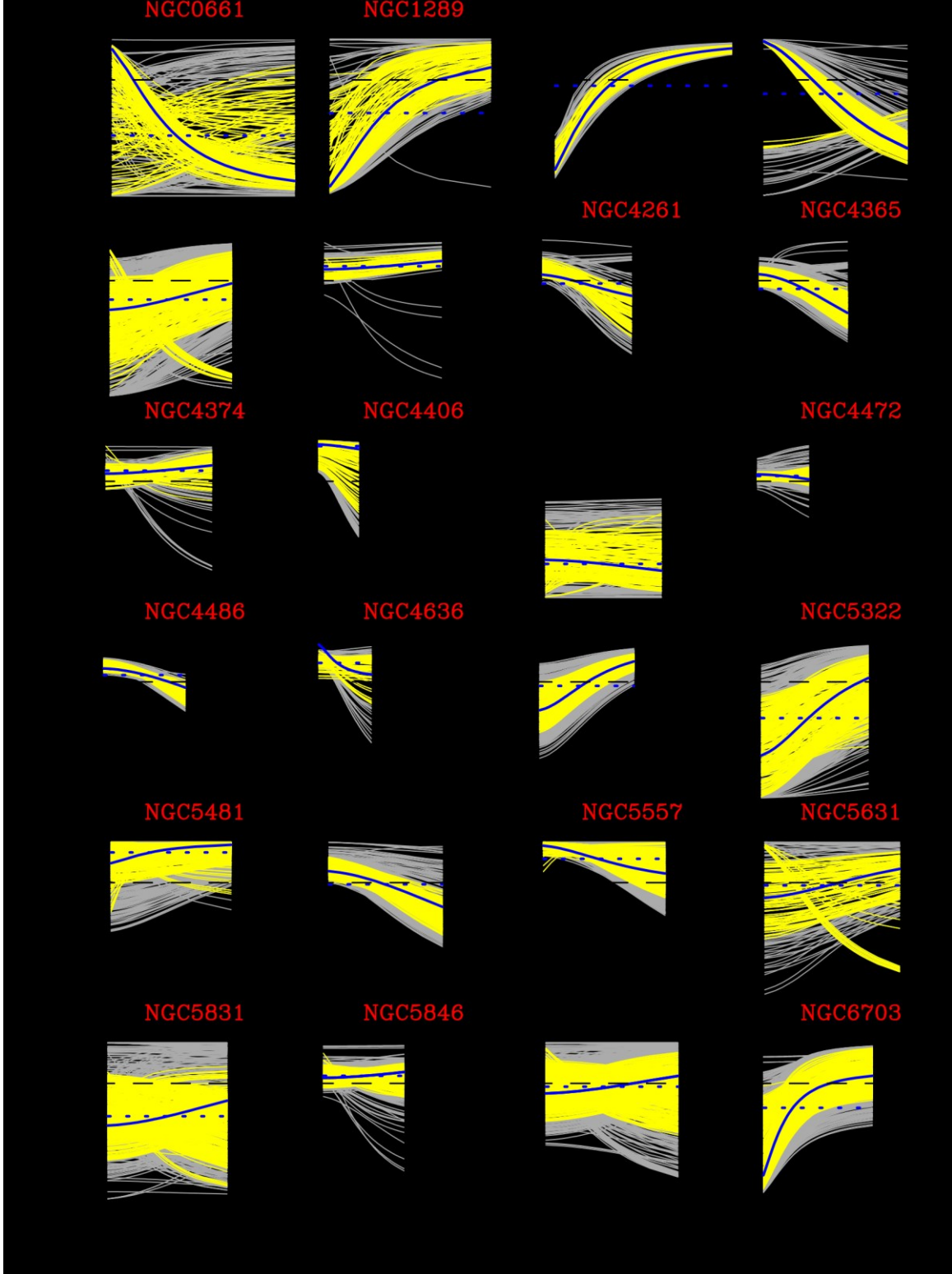probability of being (or even prefer to be) tangentially biased.

Figure 5. Same as Figure 4, but with the constraint 0 < K < 1.5; i.e., case (d) of Table 1.

Traditionally, the line-of-sight velocity dispersions are lightweighted within a projected radius R, and this light-weighted velocity dispersion, denoted by $\langle s_{los} \rangle (R)$, is

empirically approximated by a power-law relation with R, i.e., $\langle s_{los} \rangle(R) \propto R^{h_{LW}}$ (Jorgensen et al. [1995]). We calculate η_{LW} using two values, σ_e at $R = R_e$ and $\sigma_{e/8}$ at $R = R_e/8$, taken from Cappellari et al. ([2013a], [2013b]), as reproduced in Table [1]. The calculated values of η_{LW} are given in the table; they exhibit a large galaxy-to-galaxy scatter in the range $-0.13 \lesssim \eta_{LW} \lesssim 0$ with a median of $\langle h_{LW} \rangle \approx -0.06$ (Cappellari et al. [2006]). The upper panel of Figure [10] shows the fitted anisotropies with
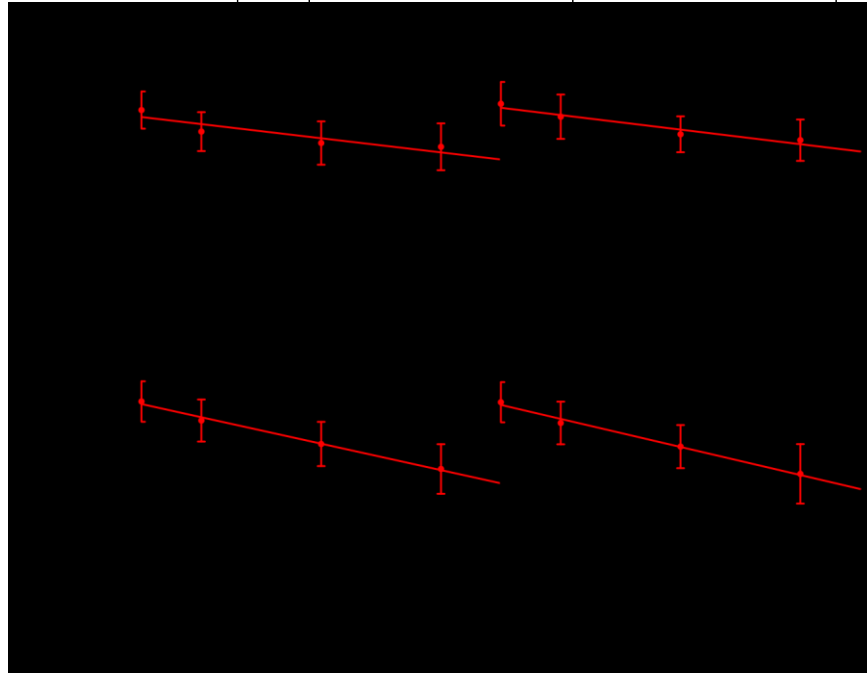
Figure 6. Median fitted anisotropies with respect to K with the gOM anisotropy model given by Equation (2). Two models (Equations (4) and (5)) of the ΛCDM (upper panels) and two models (Equations (6) and (7)) of the MOND (lower panels) are considered. Black points and lines represent all 24 pure bulges, while red ones represent the 16 SRs.

respect to η_{LW}, and the fourth panels from the top of Figure 3 show the PDFs for subsamples divided by η_{LW}. The upper lefthand panels of Figure 10 show that galaxies with steeper velocity dispersions ($\eta_{LW} > -0.08$) all appear to be radially biased when $K = 0$. The fourth left-hand panel of Figure 3 shows the shift in the value of β_m between the steeper and shallower subsamples for $K = 0$. This too can be understood in the context of the degeneracy between β and K (see Figure 2 of Bernardi et al. 2018). Indeed, when we allow for $0 < K < 1.5$, there is no longer a noticeable dependence on η_{LW} (see the upper right-hand panels of Figure 10 or the fourth right-hand panel of Figure 3).

The likely more interesting and relevant quantity is the true (as opposed to the light-weighted) slope of the $s_{los}(\ )R$ profile in the central region. This slope exhibits a greater diversity among the observed $s_{los}(\ )R$ profiles of SSBGs (see, e.g., Figure 6 of Paper I). Whereas most elliptical galaxies exhibit negative slopes (i.e., velocity dispersions usually decline with R), some observed and simulated elliptical galaxies exhibit flat or inverted $s_{los}(\ )R$ profiles near the center (i.e., they increase with R). These are referred to as central dips or depressions in the literature (see, e.g., Naab et al. 2014).

We consider the slope $h_{<0.2R_e}$ within $R < 0.2\ R_e$ defined by $s_{los}(\ )R \propto R^{h_{<0.2R_e}}$. Table 1 gives the measured values of $h_{<0.2R_e}$ based on the $s_{los}(\ )R$ profiles shown in Figure 6 of Paper I. The lower part of Figure 10 exhibits the fitted anisotropies with respect to the central slope $h_{<0.2R_e}$. In all four cases, the three SSBGs with the steepest negative slopes ($h_{<0.2R_e} < -0.1$) are all

significantly radially biased. Furthermore, for the cases of varying anisotropy (cases (b) and (d)), three SSBGs with positive or flat slopes ($h_{<0.2R_e} > -0.01$; we consider this relaxed cut considering the measurement uncertainties) are all significantly tangentially biased. The fifth panels from the top in Figure 3 show the PDFs. When the SSBGs are split into three bins of $h_{<0.2R_e}$, a systematic trend of β_m with $h_{<0.2R_e}$ is evident. When nonzero K is allowed, galaxies with positive or flat central slopes are even more tangentially biased.

The right-hand panel of Figure 8 exhibits the fitted central anisotropies, which are expected to be more directly related to the slope $h_{<0.2R_e}$. The fifth panels from the top in Figure 9 show the PDFs of β_0 for three bins of $h_{<0.2R_e}$. Indeed, the systematic trend of β_0 with $h_{<0.2R_e}$ is stronger than β_m. For the realistic case of marginalizing K over $0 < K < 1.5$, there is a clear dichotomy between the steep slope ($h_{<0.2R_e} < -0.1$) sample and the flat or inverted slope ($h_{<0.2R_e} > -0.01$) sample. The latter is tangentially biased with $\langle b_0 \rangle \approx -1.0$, while the former is radially biased with $\langle b_0 \rangle \approx 0.4$.

3.8. Correlation with Kinematry

Our results indicate that the central features of the velocity dispersions (Krajnović et al. 2011; Naab et al. 2014) in SRs are closely related to the anisotropies of the orbital distributions. To understand why, we compare $h_{<0.2R_e}$ with the kinematic features of the observed line-of-sight velocity dispersions as measured and classified by Krajnović et al. (2011) based on the

so-called kinemetry analysis. Krajnović et al. (2011) classified all 260 ATLAS[3D] ETGs into six groups based on kinematic features. According to their classification, ETGs are broadly divided into regular rotators (RRs) and nonregular rotators (NRRs). Most of the NRRs are SRs based on the angular momentum parameter λ_e of Emsellem et al. (2011). The NRRs exhibit specific features, such as kinematically distinct cores (KDCs), counterrotating cores (CRCs), and low-level (rotational) velocities (LVs). The KDCs are cores whose rotational (although the rotation itself is small for SRs) axes shift abruptly (more than 30°) from the surrounding regions. In the transition regions, there are no detectable rotations. When the shift is of the order of 180°, they are called CRCs (thus, CRCs are extreme cases of KDCs). Low-level rotation velocities

marginalizing K over $0 < K < 1.5$, the three classes show distinct features in β. The SRs with CRCs are more likely to be tangentially biased but exhibit dual possibilities, i.e., tangential and isotropic (or mildly radial). The SRs with KDCs are, on average, isotropic, with individual possibilities of radial or tangential anisotropies. The LVs/NFs are likely to be radially biased or isotropic over the IFS probed regions ($\sim R_e$) but are clearly radially biased at the center as $\beta_0 > 0$ without exception, as shown in the bottom right-hand panel of Figure 9.

These results from our modeling of SSBGs provide reasonable dynamical explanations for the observed kinematic features of SRs. The fact that three out of four CRCs have positive/flat central slopes of $s_{los}(\ )R$ profiles ("central depressions") with tangential anisotropies while one has a ("normal") negative central slope with isotropic or mildly
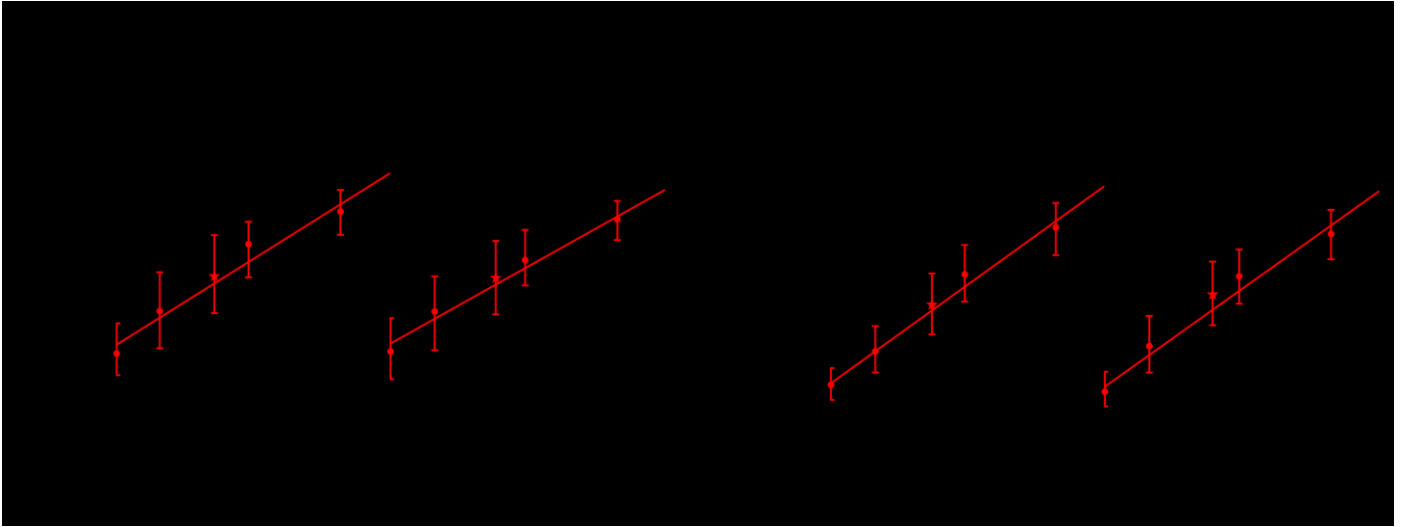

Figure 7. Median DM fractions within a sphere of $r = R_e$ with respect to K with constant anisotropies (left) and the gOM anisotropy model (right). The results are shown for both the gNFW DM model and the Einasto DM model. Black points and lines represent all 24 pure bulges, while red ones represent the 16 SRs.

throughout the observed regions are referred to as LVs. Out of our selected sample of 16 SSBGs, we have four SRs with CRCs, five with KDCs, five with LVs, and two with no features (NFs), as given in Table 1.

Figure 11 exhibits all 24 ATLAS[3D] pure bulges with respect to $h_{<0.2R_e}$, σ_e, and $M_\ast$, coding the kinematic features with different colors. The SRs with CRCs have shallower or inverted slopes compared with other kinematic classes of SRs. In particular, all three SRs with positive/flat slopes ($h_{<0.2R_e} > -0.01$) are CRCs, but not all CRCs have positive/flat slopes. Figure 11 shows the well-known fact that SRs are more massive and have higher velocity dispersions than FRs. It also shows that the kinematic features of SRs (i.e., CRCs, KDCs, and LVs) do not have preferences for σ_e or $M_\ast$. The only apparent correlation is that CRCs are biased toward the higher side of $h_{<0.2R_e}$ compared with KDCs and LVs/NFs. Then, the correlation of anisotropies with $h_{<0.2R_e}$ shown in Figure 3 implies that CRCs are likely to be more tangentially biased in the central regions.

The bottom right-hand panel of Figure 3 shows the PDFs of anisotropies for three kinematic classes of SRs. After
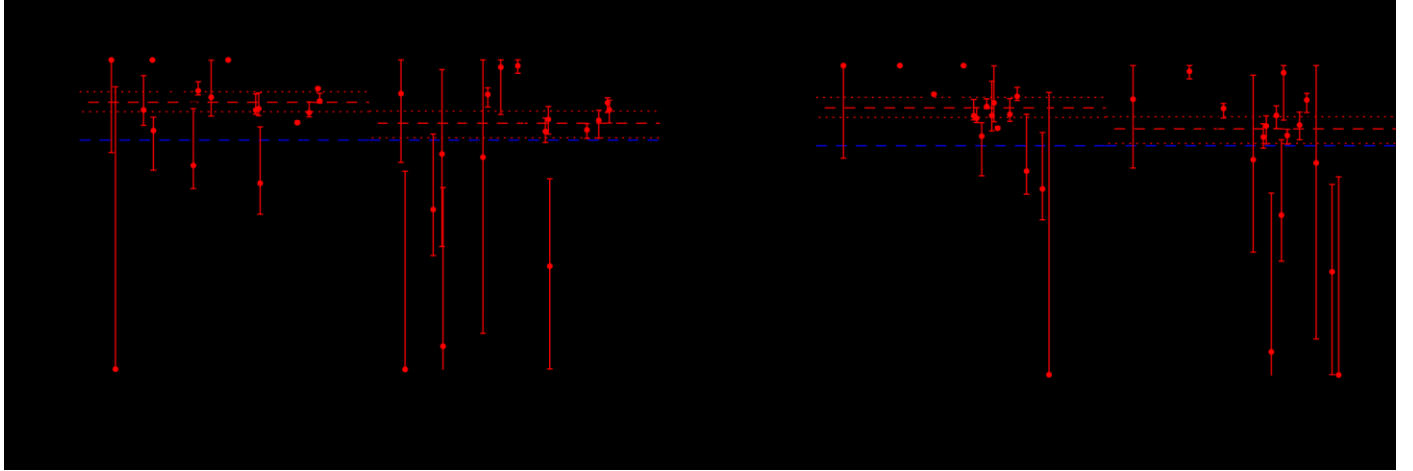
radially biased velocity dispersions (see Tables 1 and 2) hints at two distinct origins for CRCs. Those with positive/flat slopes are probably dissipationally formed cores with tangentially dominated orbits that naturally give rise to rising or flat $s_{los}(\ )R$ profiles in the central region. The CRCs with declining $s_{los}(\ )R$ profiles require another explanation. In Section 4, we use recent cosmological hydrodynamic and merger simulations to discuss the dynamical origins of CRCs.

The LVs (note that NFs are similar to LVs but with more rotations) are systems with no detectable net rotation over the regions $\sim R_e$. Systems with predominantly random (chaotic) orbits will have isotropic orbits, but our finding that LVs are more likely to be radially biased, particularly in the centers, means that the orbits have not been randomized and consist of more infalling orbits. The KDCs can be viewed as intermediate systems between CRCs and LVs; hence, both possibilities of radial and tangential biases are equally likely.

4. Comparison with Cosmological

Simulations

Recent cosmological hydrodynamic simulations of galaxy formation and evolution and galaxy merger simulations make specific predictions regarding kinematic and dynamic properties in the optical regions of galaxies and connect these properties with formation and evolution histories. Although there exist a number of state-of-the-art cosmological simulations, here we consider only those simulations that investigate kinematic features and velocity dispersion anisotropies of elliptical galaxies. A key aspect of our dynamical modeling is to allow for radial gradients in $M_{\star}/L$ in the region $R < 0.4\ R_e$ based on a host of recent reports (see Section 1). However, no cosmological simulations have allowed for such a possibility so far. Hence, comparison of our modeling results with currently available simulations is somewhat limited. As we discuss below, we find qualitative agreement but also some quantitative tension. Nevertheless, we find that such simulations are quite useful in interpreting our modeling results.

Two simulations are most relevant to the present discussion. One is the cosmological zoom-in simulation by Oser et al. (2010), and the other is the Illustris simulation (Genel et al. 2014; Vogelsberger et al. 2014a, 2014b). Based on the cosmological zoom-in simulation, Naab et al. (2014) classified 44 zoomed-in ETGs into six groups with distinctive formation paths and present-day photometric and kinematic properties.

anisotropies with respect to galaxy properties such as the light-weighted velocity dispersion σ_e (or $\sigma_{e/2}$) and the in situ stellar mass fraction, as well as (less detailed) anisotropy profiles. Such analyses have been carried out by Wu et al. (2014), Xu et al. (2017), and Li. et al. (2018).

We first discuss the overall properties of the anisotropies of SRs; then we discuss the classes grouped by kinematic features. The simulations predict that the anisotropies of all (i.e., in situ plus accreted that are observed) stellar motions for all SRs over the radial range $<R_e$ (corresponding to our probed regions) are radially biased, $\beta(r) > 0$. See Figure 18 and 19 of Röttgers et al. (2014), in which their classes C, E, and F are SRs, and also Figure 11 of Wu et al. (2014), in which larger in situ fractions can reduce $\beta(r)$ but still remain radially biased. These results are in qualitative agreement with the corresponding results of our modeling case (b), for which $M_{\star}/L$ is assumed to be constant but anisotropy is allowed to vary radially; see Figures 2 and 4. For case (b), the median radially averaged anisotropy is ≈0.2, which is in good agreement with both simulations. However, real galaxies allow tangential anisotropies; at least two galaxies in our sample (NGC 0661 and NGC 1289) prefer tangential biases (Figure 4). For a large sample of simulated ETGs, Li. et al. (2018) found a correlation of β_m with $\sigma_{e/2}$ so that lower-$\sigma_{e/2}$ galaxies may have $\beta_m < 0$. However, they do not distinguish FRs and SRs, so it is not clear whether they include any SRs having $\beta_m < 0$.

What is more striking is that when $M_{\star}/L$ gradients are

Figure 8. (Left) Central anisotropies with respect to the effective velocity dispersion σ_e of the 24 ATLAS³D pure bulges for cases (b) and (d) of Figure 2. For case (d), the higher-σ_e and lower-σ_e galaxies show a dichotomy. (Right) Central anisotropies with respect to $h_{<0.2R}$.

Röttgers et al. (2014) then investigated the stellar orbits of these simulated galaxies and provided predicted anisotropy profiles $\beta(r)$ for all six groups. The zoom-in simulation provides the finest details of the kinematic and dynamic properties of the simulated galaxies at present. One caveat of the zoom-in simulation is that their galaxies are not naturally representative of galaxies formed from a large-volume simulation. This caveat is complemented by the Illustris simulation, which is a simulation of a periodic box of 106.5 Mpc on a side. The Illustris simulation can provide distributions of averaged

allowed ($K > 0$), the median anisotropy for SRs gets close to zero, with both radial and tangential biases occurring with nearly equal probabilities. The only simulations that currently incorporate IMF-driven $M_{\star}/L$ gradients are those of Barber et al. (2018). Applying our analysis to their simulations is beyond the scope of this work but is ongoing. What follows is a discussion of the origin of this isotropy based on previously available simulation results.

When our selected 16 ATLAS[3D] SSBGs ╱ are grouped by kinematic features as identified by Krajnović et al. (2011), they are divided into three groups, i.e., four CRCs, five KDCs, and seven LVs/NFs. Three CRCs have positive/flat central slopes ("central depressions") of line-of-sight velocity dispersions, while one does not, as shown in Figure 11. The SRs with central depressions belong to class⬚C, defined by Naab et al. (2014). Orbit analyses by Röttgers et al. (2014) show that class⬚C galaxies have the lowest anisotropies among SRs (their Figure 19), although they are still radially biased. This agrees qualitatively with our anisotropy results shown in Figures 3 and 9. However, our results show that SRs with central depressions are likely to be tangentially biased or isotropic without exception, although the rest are radially biased or isotropic when $K_{\beta} = 0$ is assumed, as in simulations. For the realistic case of allowing $0 < K_{\beta} < 1.5$, SRs with central depressions are more likely to be tangentially biased. According to Naab et al. (2014), class⬚C galaxies have undergone late gas-rich major mergers. Central depressions are thought to originate from "stars that have formed from gas driven to the center of the galaxy during the merger, a process well studied in isolated binary mergers (Barnes & Hernquist 1996)." Therefore, a dissipationally formed core that is kinematically decoupled from the main body is likely to have more tangentially biased orbits. These galaxies also have relatively higher in situ fractions that are also consistent with the general trends seen in the Illustris simulation (Wu et al. 2014; Xu et al. 2017). Interestingly, the simulated galaxies with central depressions from the cosmological zoom-in simulations (Naab et al. 2014) do not exhibit CRCs, while our selected three ATLAS[3D] SRs with central depressions exhibit CRCs without exception. Note, however, that galaxy merger simulations have reproduced central depressions exhibiting CRCs (e.g., Balcells & Quinn 1990; Jesseit et al. 2007; Tsatsi et al. 2015). The remaining one SR with a CRC from our sample does not exhibit a central depression. This galaxy might be consistent with class⬚E galaxies by Naab et al. (2014), which have undergone gas-poor major mergers. These comparisons suggest that SRs with CRCs have been formed through recent major mergers with or without gas dissipation that determines the feature of central depression.

The LVs are the galaxies with no kinematic features with no significant rotations (NFs are similar to LVs but with some
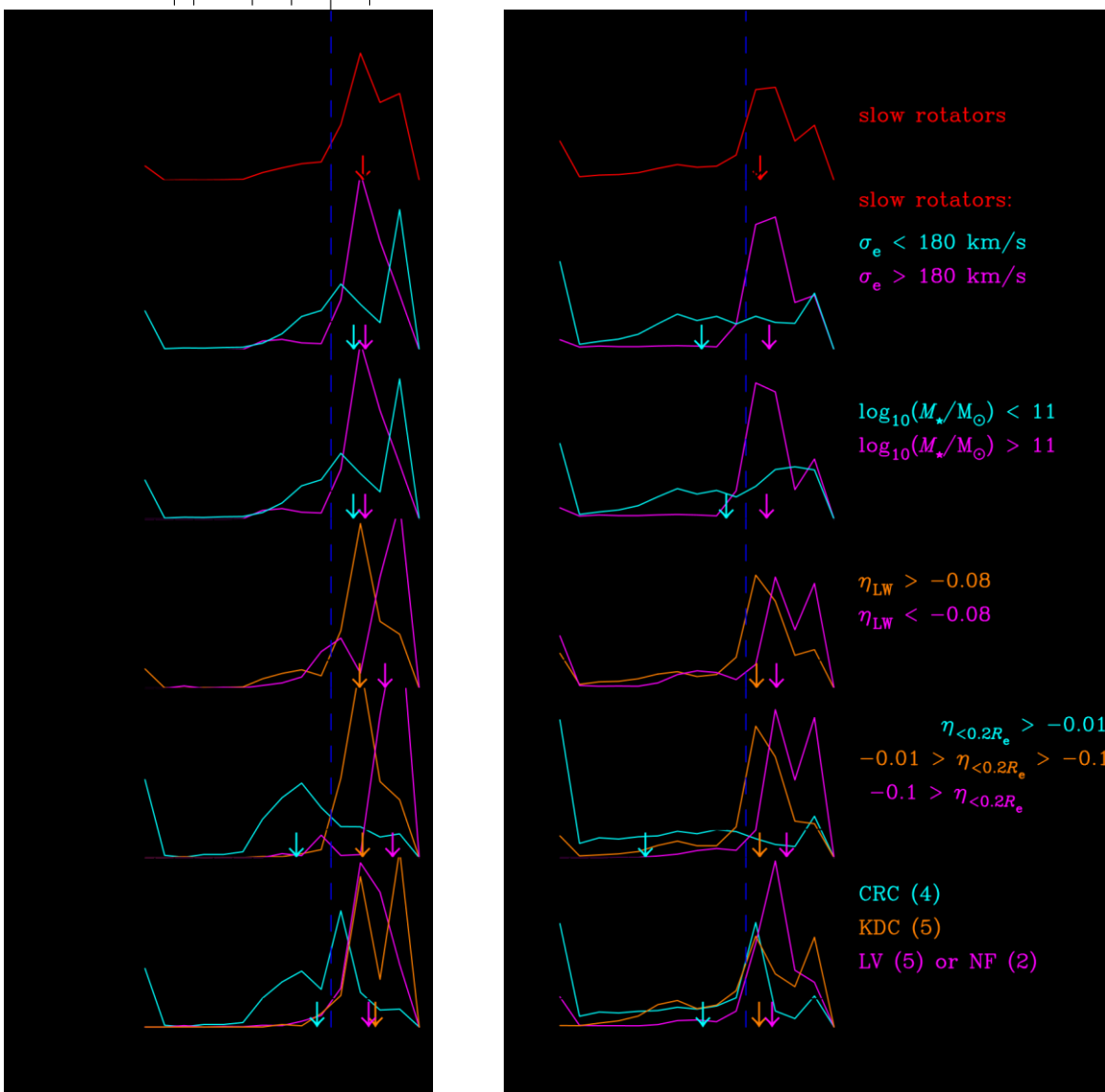
Figure 9. Same as Figure 3, but for the central anisotropy β_0.

angular momenta). These galaxies may be consistent with classes F and E of Naab et al. (2014) that have undergone only dry (minor and/or major) mergers. These galaxies have low in situ (and thus high accreted) fractions of stars. Both hydrodynamics (Röttgers et al. 2014; Wu et al. 2014; Xu et al. 2017) and merger (Hilz et al. 2012) simulations generically predict that those galaxies have radially biased orbits qualitatively consistent with our modeling results. Note here that those simulations have not considered the possibility of M$_\star$/L gradients. Our results for seven LVs/NFs with K = 0 give $\langle b_m \rangle \approx 0.4$ with a broad possible range of $-0.2 \lesssim \beta_m \lesssim 0.7$, while Figure 19 of Röttgers et al. (2014) gives $0.1 < \beta_{e/2} < 0.4$ for 14 class F/E simulated galaxies. While the predicted median is similar to our results, the simulation predicts too narrow a range of anisotropies. When M$_\star$/L gradients are allowed (the right-hand side of our Figure 3), the predicted median is lower $\left(\langle b_m \rangle \approx 0.2\right)$, but the possible range

is similar. Interestingly, our results for the central anisotropy β_0 (Figure 9) give $\beta_0 > 0$ for all LVs/NFs regardless of the assumption on M$_\star$/L gradients, while that is not the case for other kinds of SRs for $K \neq 0$ (the right-hand side of Figure 9). This is consistent with the picture that LVs/NFs do not keep dissipationally formed central components as would be lost from dry mergers. Perhaps this is not a surprising result because LVs/NFs do not contain any distinct kinematic features in the central regions by their kinematic definition. Radially biased orbits in the central regions imply that infalling orbits from accreted stars are dominating.

The KDCs are weaker versions of CRCs (or CRCs are extreme versions of KDCs). They may not exactly belong to any of the classes of SRs identified by Naab et al. (2014). They may be assigned to an intermediate class between class C and class E/F. Note that Naab et al. (2014) used just 44 simulated galaxies, which may not include the real variety of elliptical galaxies. Our results show that their median properties are close

to isotropic, but both tangential and radial ╱ biases are occurring individually.

5. Summary, Discussion, and Conclusions

We have investigated the velocity dispersion anisotropy

general ETGs. Nevertheless, they reveal key aspects of the dynamical structure of SRs and provide unique constraints on the astrophysics of galaxy formation and evolution.

Empirically, SRs tend to be more massive than FRs among ETGs. In the standard ΛCDM model, SRs are the end products of the hierarchical process of galaxy formation and evolution.

Figure 10. Same as Figure 2, but with respect to the slopes (see Table 1) η_{LW} (upper panel) and $h_{<0.2_R}$ (lower panel).
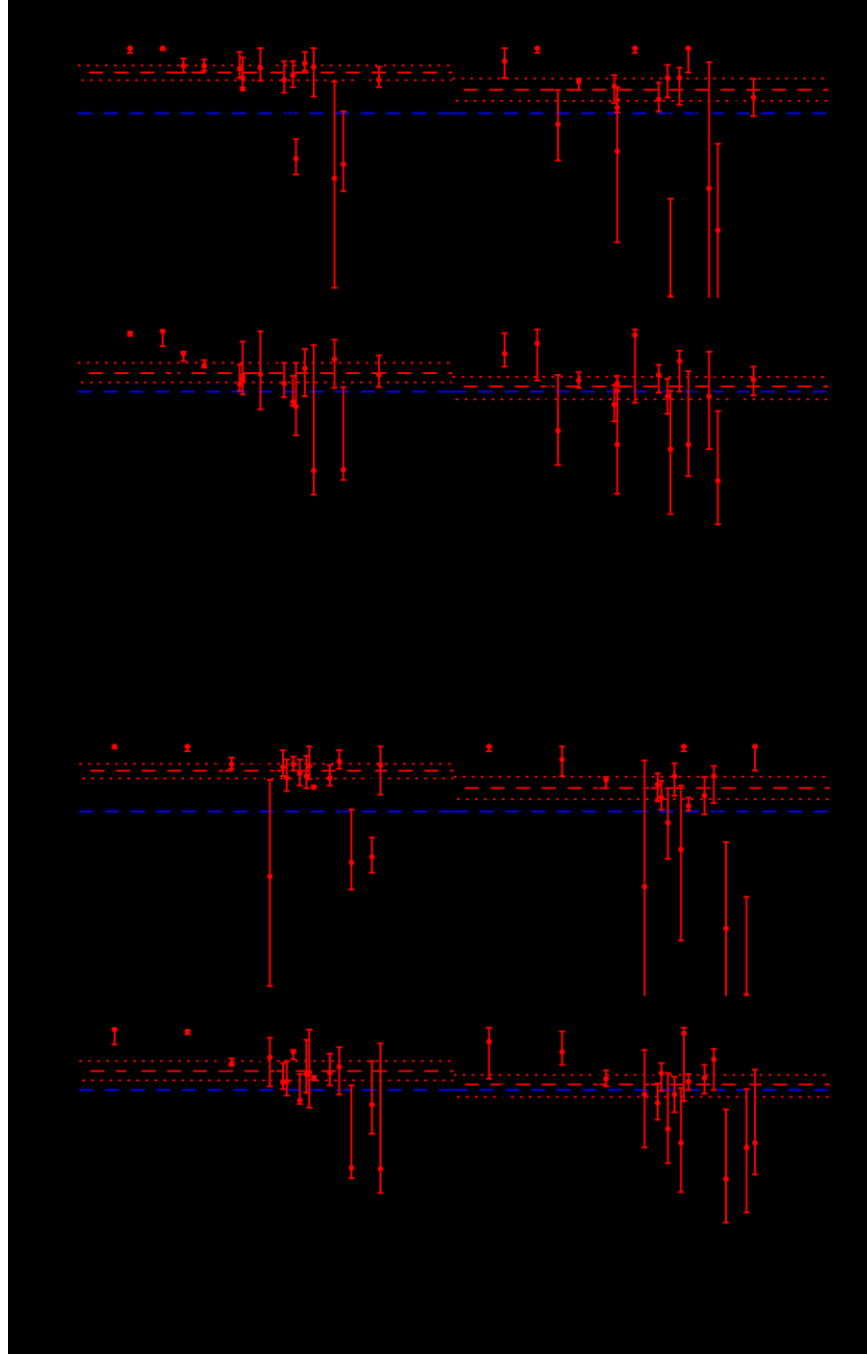
profiles of 24 ATLAS[3D] pure-bulge galaxies, paying particular attention to 16 nearly spherical SSBGs. These SSBGs constitute an extreme subset of ETGs (recall that most ETGs are now known to exhibit some rotation, as revealed by IFS studies; Emsellem et al. 2011; Krajnović et al. 2011). Therefore, our anisotropy results cannot be representative of

Therefore, their present-day orbital structure not only reveals their current dynamical state but also contains information[e]

about their dynamical (thus formation and evolution) history. Early in situ star formation, growth by gas-rich or -poor

mergers, late merger- ' ' ' ' ' ' driven in situ formation, the effects of feedback from supernovae and AGNs, etc., are all expected to influence the current dynamics of SRs.

We have estimated velocity dispersion anisotropies for these galaxies under four different assumptions (Table 1) about the anisotropy radial profile and the $M_\ast/L$ radial gradient for each of four models of DM halos or MOND IFs. For the simplest case—a constant $M_\ast/L$ and radially constant anisotropy—the observed line-of-sight velocity dispersions cannot be well fitted for ∼40% of the galaxies, and the fitted anisotropies are clearly radially biased for most of the modeled galaxies (case (a) in
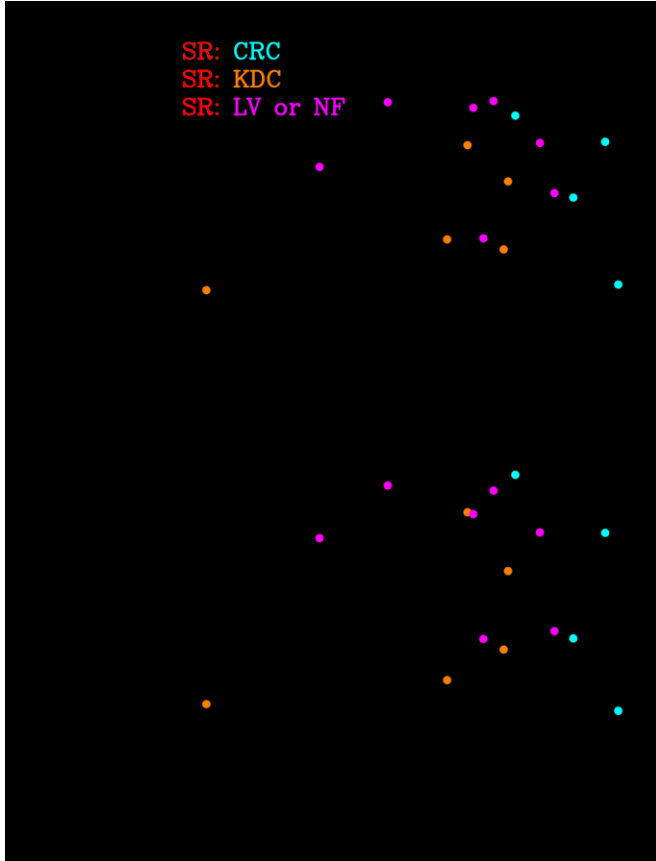

Figure 11. Kinematic features (see Table 1) of pure bulges with respect to $h_{<0.2R_e}$ (the line-of-sight velocity dispersion slope in the central region; see Table 1), σ_e (the light-weighted line-of-sight velocity dispersions within R_e taken from Cappellari et al. 2013b), and $M_\ast$ (our fitted stellar mass for case (d); see Table 1).

Table 1 and Figure 2). However, for the most realistic case— $M_\ast/L$ gradient strength K is marginalized over $0 < K < 1.5$, and anisotropy is radially varying with the flexible form of the gOM model (Equation (2))—all but one of the galaxies can be successfully modeled (and even for this one case, the line-of-sight velocity dispersions can be fitted reasonably), and the median anisotropy is close to zero; i.e., isotropy is preferred (case (d) in Table 1 and Figure 2). This holds for all four models of DM halos or MOND IFs. Here $M_\ast/L$ gradients play a key role, as shown by the systematic trend of the median

anisotropy $\langle \beta_m \rangle$ with K (Figure 6). This can be understood as follows. If $M_\ast/L$ increases toward the center but is modeled assuming there is no gradient, then isotropic velocity dispersions in the central regions would give line-of-sight velocity dispersions $s_{los}(\ )R$ that are flatter than observed (see, e.g., Figure 6 of Paper I). Radial anisotropies must then be invoked to match the observed steepening, but our results suggest that they are artifacts of ignoring $M_\ast/L$ gradients (also see Figure 2 of Bernardi et al. 2018).

Under the ΛCDM paradigm, $M_\ast/L$ gradients also have important consequences for DM distributions. If $M_\ast/L$ is larger in the central regions $(\lesssim 0.4R_e)$, then the DM contribution to the total mass distribution must be enhanced (Figure 7), while the average $M_\ast/L$ gets lowered to match the observed $s_{los}(\ )R$ profiles on scales of order R_e and larger. Thus, for SRs, the $M_\ast/L$ gradient, velocity dispersion anisotropy, and DM distribution are closely related.

Given the isotropy of SRs in the median sense, we have also investigated possible correlations of the fitted anisotropies with various other properties of galaxies. We find that the anisotropies are well correlated with the slopes of the line-of-sight velocity dispersions in the central regions ($<0.2\ R_e$) denoted by $h_{<0.2R_e}$ (Figures 8 and 10). The SRs with steeper $h_{<0.2R_e}$ are more radially anisotropic. On the other hand, SRs with flat or inverted slopes $(h_{<0.2R_e} > -0.01)$ are likely to be tangentially biased (Figure 3 and 9).

We also notice that $h_{<0.2R_e}$ correlates with the kinemetric features of SRs identified by Krajnović et al. (2011). The SRs with central depressions in the line-of-sight velocity dispersions (in the sense of having inverted or flat slopes, $h_{<0.2R_e} > -0.01$) have CRCs without exception (see Figure 11 and Table 1). However, there exist SRs with CRCs (one case out of our four SRs with CRCs) that do not have central depressions (see Krajnović et al. 2011). The SRs having KDCs, LVs, or NFs have steep slopes, $h_{<0.2R_e} < -0.0^2$ (Figure 11). The SRs grouped by three kinematic features of CRCs, KDCs, and LVs/ NFs have systematically different anisotropies (Figures 3 and 9): CRCs are tangentially biased or isotropic (or mildly radial), while LVs/NFs are radially biased or isotropic (or mildly tangential). The KDCs are close to isotropic in the median sense. This systematic trend is most pronounced in the most general and realistic modeling case (case (d) of Table 1 and Figure 2) and is at odds with the predictions by currently available simulations. Two main shortcomings of the existing simulations are the incomplete treatment of feedback from supernovae and AGNs and the use of a fixed stellar IMF. The latter means that simulations underestimate variations in $M_\ast/L$ across the galaxy population, as well as radial gradients within individual galaxies.

Although currently available ⟍
cosmological simulations cannot be directly compared with the
anisotropies obtained here for SRs, they (Naab et al. 2014;
Röttgers et al. 2014; Wu et al. 2014; Xu et al. 2017; Li. et al.
2018) can be used to interpret our anisotropy results and make
connections with the formation and evolution histories of SRs.
The SRs with CRCs have the shallowest $h_{<0.2R_e}$ (Figure 11) and
often inverted slopes ($h_{<0.2R_e} \square\ 0$). Our results show that objects
with positive slopes tend to be tangentially biased (Figures 3
and 9). Tangentially biased orbits are consistent with scenarios
in which the galaxies have undergone major gas-rich mergers
that resulted in forming cores that are decoupled from the main
bodies, as would be realized for class C galaxies by Naab et al.
(2014). However, class C simulated galaxies are not
counterrotating. Moreover, when Röttgers et al. (2014) looked
into the velocity dispersion anisotropy profiles of these
galaxies, they obtained only radially biased orbits for the
regions $\square R_e$ (although class C galaxies had the lowest
anisotropies among SRs). These discrepancies between our
results for SRs with $h_{<0.2R_e} \square\ 0$ and the class $\square$C galaxies of Naab
et al. (2014) are likely to be the consequences of the
shortcomings of the existing simulations, as pointed out above.
The CRCs without central depressions are not likely to be
tangentially biased (although our small sample includes just
one CRC without a central depression). Such galaxies may have
been formed through gas-poor major mergers, as would be
realized for class $\square$E simulated galaxies by Naab et al. (2014),
which indeed include a counterrotating case.

We find that SRs with LVs/NFs, which constitute the largest
fraction of SRs (Krajnović et al. 2011), are likely to be radially

biased. Our results are qualitatively consistent with outputs from major and/or minor gas-poor (dry) mergers (class E/F galaxies of Naab et al. 2014), which have the lowest angular momenta. However, our results allow a broader possibility, including mild tangential biases (Figures 3 and 9), while the simulations produced only the radial biases that are strongest among all classes of ETGs. The SRs with KDCs are intermediate in their kinematic features (as KDCs are weaker versions of CRCs), and our results show that their anisotropies are also intermediate. This means that SRs with KDCs are most likely to be isotropic (or mildly radially biased) in the median sense with a broad possible range.

We have explicitly allowed for $M_å/L$ gradients for $R < 0.4$ R_e in Jeans dynamical analyses of nearly spherical pure-bulge galaxies. We find that $M_å/L$ gradients have significant impacts on the inference of the velocity dispersion anisotropies. When $M_å/L$ gradients are marginalized over a reasonable range, the median anisotropy of SRs is zero, which is not the case in previous dynamical modeling results without $M_å/L$ gradients. Furthermore, SRs with different kinematic features have systematically different anisotropies. Thus, the isotropy in the median sense does not represent a dynamical property, such as chaotic orbits, but emerges as a coincidence arising from various classes. These results cannot yet be reproduced by existing cosmological simulations. Our investigations call for the need to consider $M_å/L$ gradients in dynamical modeling and cosmological simulations.

Our present work suffers from two caveats. One is the assumption of spherical symmetry, and the other is small sample size. While triaxial models would be better representations of pure-bulge galaxies, the fact that most of our selected nearly spherical pure-bulge ATLAS[3D] galaxies were successfully modeled under the spherical symmetry assumption suggests that the spherical symmetry assumption is not too unrealistic. The issue of sample size can be addressed by applying our analysis to galaxies in the MaNGA (Bundy et al. 2015) survey, which will provide an order of magnitude more galaxies like those studied here. This will allow us to apply even stricter criteria when selecting galaxies so that we can test the effects of varying selection criteria under the spherical symmetry assumption. We intend to do this in the near future. As galaxy formation simulations that include gradients become available, we will use them to test our Jeans equation–based analysis. The first simulations to incorporate IMF-driven $M_å/L$ gradients have only just been completed (Barber et al. 2018). We expect to report on the results of applying our analysis to their simulations in the near future.

In conclusion, from a range of MC models of 24 nearly spherical pure-bulge ATLAS[3D] galaxies, of which 16 are kinematic SRs, we have obtained the following results.

1. If the stellar mass-to-light ratio ($M_å/L$) is assumed to be constant within a galaxy, then one is likely to conclude that SRs have radially biased orbits, with a median

spherical anisotropy of $\langle b_m \rangle \approx 0.2$. This is in good agreement with the literature results.

2. However, if $M_å/L$ is allowed to have a radial gradient for $R < 0.4$ R_e, and the strength of this gradient is marginalized over the currently allowed range, SRs are consistent with being isotropic.

3. If $M_å/L$ gradients are allowed, then the DM contribution to the total mass distribution in the central region ($<R_e$) of SRs is $\langle f_{DM} \rangle \sim 0.35$. This is about twice as large as when gradients are ignored. As a result, SRs may in fact provide interesting probes of MOND.

4. The median isotropy of SRs appears to be a coincidencearising from a diversity of anisotropies for different kinematic SR subclasses, rather than a typical dynamical property of SRs.

5. The diverse anisotropies of SRs have much to do with thediverse slopes ($h_{<0.2R_e}$) of the line-of-sight velocity dispersions in the central regions. The SRs with very steep slopes ($h_{<0.2R_e} < -0.1$) are radially biased, while SRs with flat or inverted slopes ($h_{<0.2R_e} > -0.01$, representing central depressions) are tangentially biased.

6. Three out of four SRs with CRCs exhibit centraldepressions and thus are tangentially biased. One SR with a CRC that does not exhibit central depression is not tangentially biased. The SRs with CRCs may have been formed through major mergers, and the amount of gas involved (i.e., whether gas-rich or gas-poor) may have influenced the presence or lack of central depression.

7. The SRs with LVs or NFs are likely to be radially biased.They may have been formed through gas-poor major and/or minor mergers.

8. The SRs with KDCs are intermediate between SRs withCRCs and SRs with LVs. Their velocity dispersions are close to the isotropy in the median sense.

ORCID iDs

Kyu-Hyun Chae https://orcid.org/0000-0002-6016-2736
Ravi K. Sheth https://orcid.org/0000-0002-2330-0917

References

Alton, P. D., Smith, R. J., & Lucey, J. R. 2017, MNRAS, 468, 1594
Alton, P. D., Smith, R. J., & Lucey, J. R. 2018, MNRAS, 478, 4464
Balcells, M., & Quinn, P. J. 1990, ApJ, 361, 381

Barber, C, Crain, R. A., & Schaye, J. 2018, MNRAS, 479, 5448

Barnes, J. E., & Hernquist, L. 1996, ApJ, 471, 115

Bernardi, M., Sheth, R. K., Dominguez-Sanchez, H., et al. 2018, MNRAS, 477, 2560

Binney, J, & Mamon, G. A. 1982, MNRAS, 200, 361

Binney, J., & Tremaine, S. 2008, Galactic Dynamics (2nd ed.; Princeton, NJ: Princeton Univ. Press)

Bois, M., Emsellem, E., Bournaud, F., et al. 2011, MNRAS, 416, 1654

Bundy, K., Bershady, M. A., Law, D. R., et al. 2015, ApJ, 798, 7

Cappellari, M. 2016, ARA&A, 54, 597

Cappellari, M., Bacon, R., Bureau, M., et al. 2006, MNRAS, 366, 1126

Cappellari, M., Emsellem, E., Bacon, R., et al. 2007, MNRAS, 379, 418

Cappellari, M., Emsellem, E., Krajnović, D., et al. 2011, MNRAS, 413, 813

Cappellari, M., McDermid, R. M., Alatalo, K., et al. 2013a, MNRAS, 432, 1862

Cappellari, M., Scott, N., Alatalo, K., et al. 2013b, MNRAS, 432, 1709 Chae, K.-H., Bernardi, M., & Sheth, R. K. 2018, ApJ, 860, 81, (Paper I)

Chae, K.-H., Bernardi, M., Sheth, R. K., & Gong, I.-T. 2019, ApJ, submitted

Davis, T. A., & McDermid, R. M. 2017, MNRAS, 464, 453 de Zeeuw, P. T., Bureau, M., Emsellem, E., et al. 2002, MNRAS, 329, 513

de Zeeuw, T. 1985, MNRAS, 216, 273

Einasto, J. 1965, TrAlm, 5, 87

Emsellem, E., Cappellari, M., Krajnović, D., et al. 2007, MNRAS, 379, 401

Emsellem, E., Cappellari, M., Krajnović, D., et al. 2011, MNRAS, 414, 888

Famaey, B., & Binney, J. 2005, MNRAS, 363, 603

Gebhardt, K., Richstone, D., Tremaine, S., et al. 2003, ApJ, 583, 92

Genel, S., Vogelsberger, M., Springel, V., et al. 2014, MNRAS, 445, 175

Gerhard, O., Kronawitter, A., Saglia, R. P., & Bender, R. 2001, AJ, 121, 1936

Hilz, M., Naab, T., Ostriker, J. P., et al. 2012, MNRAS, 425, 3119

Janz, J., Cappellari, M., Romanowsky, A. J., et al. 2016, MNRAS, 461, 2367

Jesseit, R., Naab, T., & Burkert, A. 2005, MNRAS, 360, 1185

Jesseit, R., Naab, T., Peletier, R. F., & Burkert, A. 2007, MNRAS, 376, 997

Jorgensen, I., Franx, M., & Kjaergaard, P. 1995, MNRAS, 276, 1341

Kent, S. M. 1987, AJ, 93, 816

Koopmans, L. V. E., Bolton, A., Treu, T., et al. 2009, ApJL, 703, L51

Kormendy, J. 2008, Galactic Bulges, Astrophysics and Space Science Library, Vol. 418 (Cham: Springer International),431

Krajnović, D., Alatalo, K., Blitz, L., et al. 2013, MNRAS, 432, 1768

Krajnović, D., Bacon, R., Cappellari, M., et al. 2008, MNRAS, 390, 93

Krajnović, D., Cappellari, M., Emsellem, E., McDermid, R. M., & de Zeeuw, P. T. 2005, MNRAS, 357, 1113

Krajnović, D., Emsellem, E., Cappellari, M., et al. 2011, MNRAS, 414, 2923

La Barbera, F., Vazdekis, A., Ferreras, I., et al. 2016, MNRAS, 457, 1468

Li., H., Mao, S., Emsellem, E., et al. 2018, MNRAS, 473, 1489

Martín-Navarro, I., La Barbera, F., Vazdekis, A., Falcón-Barroso, J., & Ferreras, I. 2015, MNRAS, 447, 1033 McGaugh, S. 2008, ApJ, 683, 137

Merritt, D. 1985, AJ, 90, 1027

Merritt, D., Graham, A. W., Moore, B., Diemand, J., & Terzić, B. 2006, AJ, 132, 2685

Milgrom, M. 1983, ApJ, 270, 371

Mo, H., van den Bosch, F. C., & White, S. 2010, Galaxy Formation and Evolution (Cambridge: Cambridge Univ. Press)

Naab, T., Oser, L., Emsellem, E., et al. 2014, MNRAS, 444, 3357

Navarro, J. F., Frenk, C. S., & White, S. D. M. 1997, ApJ, 490, 493

Navarro, J. F., Ludlow, A., Springel, V., et al. 2010, MNRAS, 402, 21

Oldham, L., & Auger, M. 2018, MNRAS, 474, 4169

Oser, L., Ostriker, J. P., Naab, T., Johansson, P. H., & Burkert, A. 2010, ApJ, 725, 2312

Osipkov, L. P. 1979, PAZh, 5, 77

Richstone, D. O., & Tremaine, S. 1988, ApJ, 327, 82

Röttgers, B., Naab, T., & Oser, L. 2014, MNRAS, 445, 1065

Sarzi, M., Spiniello, C., La Barbera, F., Krajnović, D., & van den Bosch, R. 2018, MNRAS, 478, 4084

Sérsic, J. L. 1968, Atlas de Galaxias Australes (Córdoba: Observatorio Astronómico)

Sonnenfeld, A., Leauthaud, A., Auger, M. W., et al. 2018, MNRAS, 481, 164

Statler, T. S. 1987, ApJ, 321, 113

Thomas, J., Saglia, R. P., Bender, R., et al. 2007, MNRAS, 382, 657

Tsatsi, A., Macció, A. V., van de Ven, G., & Moster, B. P. 2015, ApJL, 802, L3 van der Marel, R. P., Cretton, N., de Zeeuw, P. T., & Rix, H.-W. 1998, ApJ, 493, 613 van Dokkum, P., Conroy, C., Villaume, A., Brodie, J., & Romanowsky, A. J. 2017, ApJ, 841, 68

Vogelsberger, M., Genel, S., Springel, V., et al. 2014a, MNRAS, 444, 1518

Vogelsberger, M., Genel, S., Springel, V., et al. 2014b, Natur, 509, 177

Wu, X., Gerhard, O., Naab, T., et al. 2014, MNRAS, 438, 2701 Xu, D., Springel, V., Sluse, D., et al. 2017, MNRAS, 469, 1824